U.PORTO

FEUP FACULDADE DE ENGENHARIA
UNIVERSIDADE DO PORTO

MASTER'S IN ENVIRONMENTAL ENGINEERING 2021/2022

ADVANCED COMPUTATIONAL METHODS APPLIED TO THE DESIGN OF PRIMARY SETTLERS

MARIA CAROLINA SEQUEIRA RODRIGUES FERREIRA DUARTE

Dissertation submitted for the degree of

MASTER ON ENVIRONMENTAL ENGINEERING

Supervisor at the University:
Ricardo Nogueira dos Santos, Auxiliary Researcher, Faculdade de Engenharia da Universidade do Porto

Co-advisor at University:
Anna Maria Karpinska Portela; Senior Modelling Engineer; Operational Planning and Improvement, Wastewater Operations, Southern Water, UK

Margarida Abrunhosa de Brito, Post-Doctoral Researcher, Chemical Engineering Department, Faculdade de Engenharia da Universidade do Porto

Agradecimentos

Tenho plena consciência de que a presente dissertação de mestrado não teria sido concretizada sem o apoio de várias pessoas que, de forma direta ou indireta, contribuíram para a sua realização e me ajudaram a superar obstáculos e dificuldades. Assim, gostaria de agradecer de modo particular algumas destas pessoas especiais.

Em primeiro lugar, ao meu orientador Professor Doutor Ricardo Jorge Santos, pela sua total disponibilidade durante estes meses de trabalho, pelo constante incentivo e por toda a partilha de conhecimento e experiência. A criatividade e motivação do Professor Ricardo são contagiantes e a sua confiança no meu trabalho incentivaram-me a nunca desistir face aos mais variados problemas.

Às minhas coorientadoras, Doutora Margarida Brito e Doutora Anna Karpinska Portela, pelo seu apoio, atenção e ajuda nos mais variados aspetos, quer fossem estes de natureza técnica quer de escrita e por todos os seus conselhos valiosos.

Ao meu pai, Zené, por toda a ajuda, incentivo e inspiração. Por me fazer pensar em tudo o que apresento com uma visão mais objetiva e por me ensinar que há sempre solução para tudo se pensarmos de forma clara e coerente.

À minha mãe, Paula, por todo o amor e apoio, por acreditar sempre em mim e por me mostrar que com trabalho e esforço tudo se consegue.

Aos meus irmãos, João Pedro, Francisco e Maria João, e aos meus sobrinhos, Nicolau, Zé Maria e Manel, por todos os sorrisos e alegria e por estarem sempre ao meu lado.

Ao meu Francisco, por todo o carinho, pela partilha não só das minhas conquistas como dos meus momentos mais difíceis, por estar sempre presente e me motivar a ser melhor.

Às minhas melhores amigas, Ritinha, Kika, Lopo e Inês, pela maravilhosa coletânea de memórias que levo comigo destes últimos anos.

Aos meus amigos de faculdade, Maria Luísa, Daniel e Luís, por todos os momentos e partilhas.

Por fim, um carinhoso agradecimento a toda à minha família e amigos pela amizade e motivação que nunca me faltou e que foi fundamental ao longo destes longos cinco anos de curso.

Este trabalho foi em parte financiado por: LA/P/0045/2020 (ALiCE), UIDB/50020/2020 e UIDP/50020/2020 (LSRE-LCM) financiado por fundos nacionais através de FCT/MCTES (PISSAC).

FCT Fundação para a Ciência e a Tecnologia
MINISTÉRIO DA CIÊNCIA, TECNOLOGIA E ENSINO SUPERIOR

REPÚBLICA PORTUGUESA

Abstract

Recent environmental goals make the application of the existing design guidelines fall short in the design of new and more efficient primary settling tanks (PST) of wastewater treatment plants (WWTP) due to their lack of flexibility. This work concerns the enhancement of the efficiency of the design of a circular primary settling tank using advanced computational methods.

In this work, the hydrodynamics in a circular primary settling tank geometry is studied using two-dimensional, 2D, Computational Fluid Dynamics simulations. The PST model in which these studies are based was provided by an English South Coast WWTP, as well as the data used in the simulations.

For this study, five different inlet designs were tested, for two different influent velocities, to obtain data regarding these inlet variation influence on tank velocities, turbulent kinetic energy, and flowrate streamlines in the PST.

For a sedimentation study, six particle's diameters injections were simulated to the provided PST model, using the Discrete Particle Model (DPM) from Ansys Fluent, to analyze the settling behavior in the tank and the correlation between the particle size and the sedimentation processes within the PST.

A Settling Expedite Assessment Method (SEAM) was also developed through the course of this work. This method's purpose is to simplify the correlation between the velocity and the path lines in the tank and the diameter of the discrete settling matter, in order to predict the settled matter percentage with only the particle size and a hydraulic simulation of the flow in the PST.

This work will contribute to further know-how about PST's design optimization using CFD for better sedimentation efficiency that can be applied to wastewater treatment plant.

Keywords (theme): Wastewater treatment, primary settling tanks, computational fluid dynamics, sedimentation, particles

Resumo

As políticas e objetivos ambientais atuais constituem um desafio para as estações de tratamento de águas residuais, ETARs. É requerido a estas instalações um aumento de eficiência impossível de alcançam com base nas diretrizes de dimensionamento existentes na conceção de tanques de sedimentação primária. São assim necessários novos e mais eficientes tanques de decantação primária. Este trabalho pretende contribuir para a melhoria da eficiência do dimensionamento de tanques de decantação primário circulares com recurso a métodos computacionais avançados.

Neste trabalho, a geometria de um tanque de sedimentação primária circular é estudada usando simulações bidimensionais, 2D, de Computação de Fluidos Dinâmicos, CFD. O modelo no qual esses estudos se baseiam foi fornecido por uma ETAR da Costa Sul de Inglaterra, assim como os dados utilizados nas simulações.

Para este estudo, cinco desenhos diferentes da zona de entrada do tanque foram testados, para duas velocidades de afluente diferentes, de forma a obter dados sobre a influência dessas geometrias da entrada nas velocidades do tanque, energia cinética turbulenta e linhas de fluxo no sedimentador.

Para a realização de um estudo de sedimentação discreta, foram simuladas injeções de partículas com seis diâmetros para o modelo de sedimentador fornecido, usando o método DPM do Ansys/Fluent, para analisar o comportamento de sedimentação no tanque e a correlação entre o tamanho das partículas e os processos de sedimentação dentro do sedimentador.

Ao longo deste trabalho também foi desenvolvido um Método Expedito de Avaliação de Sedimentação, SEAM. O objetivo deste método é simplificar a correlação entre a velocidade e as linhas de trajetória no tanque e o diâmetro da matéria discreta que sedimenta, a fim de prever a percentagem de matéria sedimentada tendo apenas o diâmetro de partícula e uma simulação hidráulica do escoamento no sedimentador.

Este trabalho contribuirá para aprofundar o conhecimento sobre a otimização do projeto e dimensionamento de sedimentadores primários para aplicação em ETARs, através da aplicação de CFD de forma a melhorar a eficiência de sedimentação.

Palavras-chave: Estações de tratamento de águas Residuais, Tanques de decantação primária, Computação em fluidos dinâmicos, sedimentação, partículas

Declaration

I hereby declare, under word of honour, that this work is original and that all non-original contributions is indicated, and due reference is given to the author and source

Maria Carolina Sequeira Rodrigues Ferreira Duarte

julho 2022

Index

List of Figures

List of Tables

Notation and Glossary

C_D	Drag coefficient	
D	Diameter	m
G_b	Generation of turbulent energy from buoyancy	$\text{kg m}^{-1} \cdot \text{s}^{-3}$
G_k	Generation of turbulent energy due to mean velocity gradients	$\text{kg m}^{-1} \cdot \text{s}^{-3}$
$\vec{F}$	Additional force	N
F_D	Drag force	N
I_t	Turbulent Intensity	
k	Turbulent Kinetic Energy	$\text{m}^2 \cdot \text{s}^{-2}$
L	Length	m
m_p	Particle mass	kg
r	Radial coordinate	m
R	Radius	m
R_ε	Addition term	
Re	Reynolds number	
Re_r	Relative Reynolds number	
s_ε	User defined source term	$\text{kg m}^{-1} \cdot \text{s}^{-4}$
s_k	User defined source term	$\text{kg m}^{-1} \cdot \text{s}^{-3}$
V	Water displaced by a particle	m^3
W_B	Buoyant weight	
x	Axial coordinate	m
y	Space coordinate	m
y^*	Wall y star	
Y_M	Fluctuating dilatation in compressible turbulence	$\text{kg m}^{-1} \cdot \text{s}^{-3}$

Greek Letters

α_ε	Inverse Prandlt number for ε	
α_k	Inverse Prandlt number for k	
δ	Path line	
Δh	Space between path lines	m
Δt	Time interval	s
ε	Turbulent Energy Dissipation	$\text{m}^2 \cdot \text{s}^{-3}$
η	Effectiveness factor	
θ	Detention time	h

μ	Dynamic viscosity	$\mathrm{Pa \cdot s}$
μ_{eff}	Effective dynamic viscosity	$\mathrm{Pa \cdot s}$
μ_t	Turbulent Viscosity	$\mathrm{Pa \cdot s}$
ρ	Density	$\mathrm{kg \cdot m^{-3}}$
ρ_p	Specific mass of a particle	$\mathrm{kg \cdot m^{-3}}$
ρ_f	Specific mass of a fluid	$\mathrm{kg \cdot m^{-3}}$
ν	Kinematic viscosity	$\mathrm{m^2 \cdot s^{-1}}$
τ_r	Particle relaxation time	
υ	Velocity magnitude	$\mathrm{m} \cdot s^{-1}$
υ_H	Horizontal velocity	$\mathrm{m} \cdot s^{-1}$
υ_o	Overflow rate	$\mathrm{m^3/m^2} \cdot d^{-1}$
υ_δ	Terminal velocity	$\mathrm{m} \cdot s^{-1}$
υ_x	Axial velocity	$\mathrm{m} \cdot s^{-1}$
υ_r	Radial velocity	$\mathrm{m} \cdot s^{-1}$
$\vec{\upsilon}$	Velocity vector	$\mathrm{m} \cdot s^{-1}$
ϕ	Particle	

Indexes

c	Influent velocity
i	Particle identification number
j	Inlet design
n	Path line number
k	Particle ID

List of Acronyms

2D	Two-dimensional
AD	Anaerobic Digestion
ASP	Activated Sludge Process
BOD	Biochemical Oxygen Demand
CAPS	Chemically Assisted Primary Sedimentation
CFD	Computational Fluid Dynamic
DPM	Discrete Particle Model
DS	Dry Solids
MLSS	Mixed Liquor Suspended Solids
PS	Primary Sludge

PSD	Particle Size Distribution
PST	Primary Settling Tanks
RAS	Return Activated Sludge
SEAM	Settling Expedite Assessment Method
SS	Suspended Solids
SST	Secondary Settling Tank
WAS	Waste Activated Sludge
WWTP	Wastewater Treatment Plant

1 Introduction

1.1 Motivation and Relevance

Primary settling tanks (PSTs) are sedimentation basins used in the mechanical treatment stage at wastewaters in Wastewater Treatment Plants (WWTPs). PSTs consist of units designed for the separation of organic, inorganic, and inert debris from the influent water.

The design of PSTs requires the optimization of geometrical configuration, such as depth, inlet and outlet, and mechanisms of collecting sludges and scum. The optimization will guarantee to control the biological activities, maximize the flocculation, and minimize undesired hydraulic phenomena, such as eddy and density currents. The designs of the inlet zone, settling zone and outlet zone are of outmost importance for PSTs because good sedimentation performance is widely dependent on these zones. Inlet flow conditions and inlet zone design must be optimized in order to promote the sediment's divergence from the flow and settling to the bottom of PSTs.

In WWTPs, the project of these units are based on parameters listed and dimensioned in the literature (Metcalf and Eddy 2014; Hendricks 2016). The further environmental sustainability goals make the adaptation of the existing, rigid construction guidelines fall short of flexibility for the conceptualization of new and more efficient PST designs.

In this work, numerical modelling solutions were used to study phenomena occurring in the PST aiming at the enhancement of hydraulic design. The real-scale PST design and the performance data used in the simulations were kindly provided by a medium sized WWTP located on South Coast of England.

For this study, five different designs of the flow entrance region were tested, for two different influent velocities in the PST. These conditions were used to obtain data regarding the influence of the inlet region design on the tank velocities, turbulent kinetic energy, turbulent energy dissipation, and flow streamlines.

For the sedimentation study, six diameters of particles injected in the PST were simulated. The particles paths enabled assessing the settling behavior in the tank and to set the correlation between the particle size and the sedimentation processes within the PST.

Nowadays, the need to optimize and explore solutions passes through the reinvention and actualization of already existing systems, such as WWTP to fulfill more stringent requirements and environmental strategies. As such, computational fluid dynamics, CFD, becomes an important tool for the conception of more efficient and accurate settling tanks.

1.2 Thesis Objectives and Layout

The objectives of this thesis are the description of the operation and importance of a PST, the review of design guidelines for PSTs and the development of numerical modeling tools for a more scientifically accurate primary sedimentation unit process design.

To fulfill the objectives mentioned above, the layout of the work is as follows.

Chapter 2 aims to summarize past studies regarding the application of Computational Fluid Models for the design of settlers and to introduce essential concepts used in this dissertation. This chapter was divided in three sections: Settlers for Wastewater Treatment (Section 2.1), Settler design (Section 2.2), and Computational Fluid Dynamics applied to the design of primary settling tanks (Section 2.3).

Chapter 3, describes the setup of a two-dimensional CFD simulation of a circular primary settler: the physical domain (Section 3.1), the governing equations and boundary conditions (Section 3.2) , the numerical solution with the methods and criteria applied (Section 3.3), the grid independence test carried out to validate the mesh applied to the tests and study that followed (Section 3.4) and lastly the description of the CFD simulations carried out for the inlet design study (Section 3.5) and the particle sedimentation study (Section 3.6).

The performed simulation's results are reported in chapter 4: the CFD simulation's results for the inlet study (Section 4.1), the DPM simulation's results (Section 4.2) and lastly the description of a Settling Expedite Assessment Method created through the course of this work, the comparison of this method's results with the DPM simulation's result and its application to a case study (Section 4.3).

Chapter 5 presents the conclusions taken throughout the course of the elaboration of this work and section 5.1 presents the limitations and the considerations for future works.

This work has three appendixes, A, B and C. Appendix A describes the Stoke's Law, considered in some studies made on this thesis; Appendix B describes the simplified method for the assessment of settled particles developed in this work, SEAM and Appendix C shows the parameter values of SEAM for a studied velocity.

2 Context and State of the art

Water is an essential and necessary good, being the main component of living organisms and the most used natural resource. However, the scarcity of drinking water and water pollution are some of the biggest problems faced nowadays. Previously, due to the visible abundance of this resource on the planet, the population took it for granted, using it in an unmeasurable way. In the recent years, modern and more informed and conscious society finds itself concerned with this matter looking to find solutions to this problem (European Environmental Agency 2018).

The day-to-day water utilised, discarded, and treated makes up the Urban Water Cycle, showed in Figure 1.

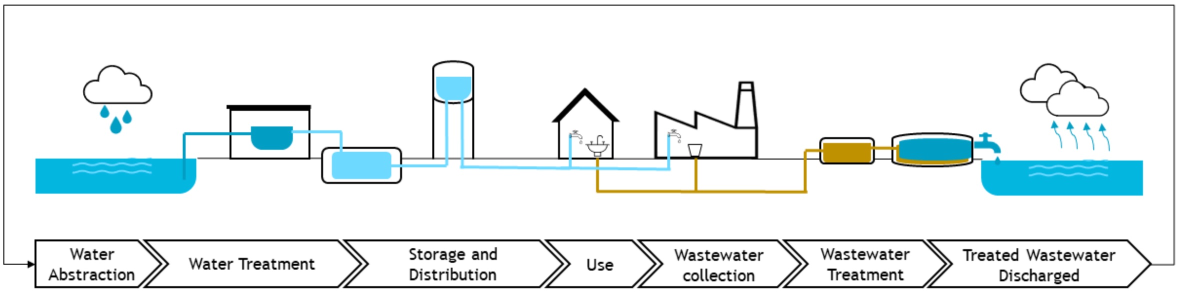

Figure 1 - Urban Water Cycle.

Nowadays, adaptation to climate change and water- energy- food nexus enforce a range of initiatives and mitigating actions in the wastewater sector, aiming towards Net-Zero Energy and Net-Zero Carbon targets. Accordingly, the process of converting many WWTPs into energy-/carbon- and climate-neutral facilities relies on enabling energy efficiency opportunities, use of renewable energy sources and elimination of the fugitive emissions. In this context, Anaerobic Digestion (AD) is an important unit process producing renewable energy from the sludge to offset power drawn from grid, generated mostly from the fossil fuels, and required to operate WWTP. One of the established methods to increase biogas (methane) yield in AD relies on the optimum primary sludge to secondary sludge ratio in the feed to digester.

This dissertation focus is on the use of advanced computational methods for Primary Sedimentation Tanks design, allowing to optimise and enhance primary sludge separation from wastewater, shifting the WWTPs energy balance towards neutrality (Patziger et al. 2016; International Energy Agency 2021; Cheng Sun 2022).

2.1 Settlers for Wastewater Treatment

A WWTP is a facility with combination of physical, mechanical, chemical and biological processes aimed to wastewater treatment through the removal of pollutants and other substances from domestic and industrial influent water (Hreiz, Latifi, and Roche 2015). A typical WWTP comprises a treatment train with the following described phases:

- Preliminary treatment – responsible for the removal of coarse solids and other larger materials found in the influent wastewater;
- Primary treatment – designed to remove organic and inorganic suspended solids, by means of sedimentation and flocculation processes;
- Secondary treatment – based on the biological metabolic processes of pollutant removal carried out by active biomass, which is either suspended within the wastewater in the tank (suspended growth process or Activated Sludge Process - ASP) or attached forming biofilm (e.g., trickling filters or membrane reactors);
- Tertiary treatment – is a polishing, “add-on” treatment phase, to obtain a final effluent of different, higher quality, to be discharged into natural water bodies (Sonune and Ghate 2004). WWTPs are usually equipped with two different sedimentation tanks:
    - a Primary Sedimentation Tank (PST) for settleable organic and inorganic matter removal in the primary phase of treatment, which operation results in a product: effluent water that follows to the secondary treatment, and a by-product: Primary Sludge (PS);
    - and a Secondary Sedimentation Tank (SST) for biological floc separation, in the secondary phase of treatment that results in a treated effluent and its by-product, part of which is recycled to the head of ASP as a Return Activated Sludge (RAS) and the remaining excess is removed as Waste Activated Sludge (WAS).

The location of the PST and SST within conventional biological WWTP flow diagram is shown in Figure 2.

The required PST performance is determined to a larger extent by the size of the WWTP, crude sewage characteristics, type (physical, chemical, or biological) and operational condition of the downstream water- and sludge- treatment processes, as well as by the treatment goals required by the regulator, i.e. final effluent quality (Patziger and Kiss 2015). As a rule of thumb, well designed PST should be able to remove 50-70 % of the suspended solids (SS) and 25-40% of the Biochemical Oxygen Demand (BOD).

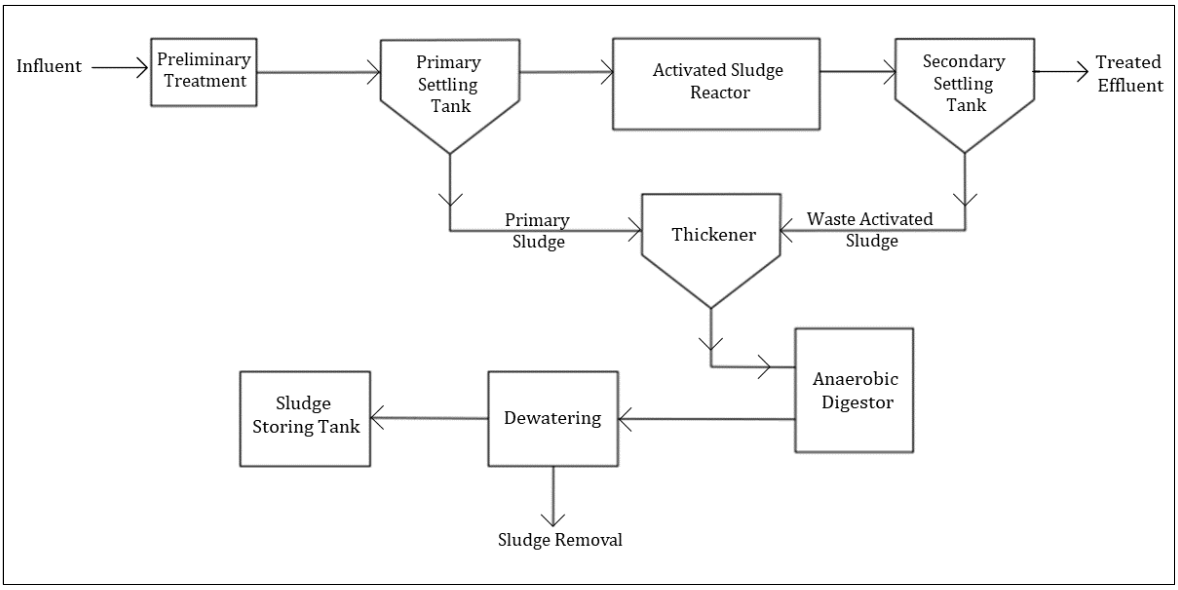

Figure 2 - Simplified Scheme of Wastewater Treatment Plant.

The solids reduction upstream the ASP is important from the point of view of the sludge age control, and hence the Mixed Liquor Suspended Solids (MLSS) concentrations in the aeration basin required for the carbonaceous (floc-forming) and nitrification processes. At the same time, BOD load reduction to the ASP has a significant impact on the oxygen demand by AS biomass and consequently on decrease of the energy demand for aeration. This results in a reduction of the operation expenditure (OPEX) costs off the WWTP in line of the Net Zero Energy strategy goals (Margarit Bel, Retana Pastor, and Malfeito Sanchez 2017).

One of the techniques applied to improve the efficiency of primary sedimentation is to dose coagulants upstream the PST, referred either as Chemically Assisted Primary Sedimentation (CAPS) or Chemically Enhanced Primary Sedimentation. Depending on the final effluent criteria, higher coagulant doses are typically used to achieve CAPS dosing, which could result in a high phosphorus removal via precipitation.

CAPS allows to achieve enhanced SS and BOD removal within the PS, decreasing simultaneously secondary sludge production, and hence WAS volume. The latter one results in additional OPEX savings associated with the polymer demand for WAS thickening. Due to its composition, PS has higher calorific value for AD than WAS made up of dead biomass cells. PS is also easier to thicken and achieve the optimum dry solids percentage (% DS) for AD. Accordingly, optimized PS removal allows to modify PS/WAS ratio in the digester feed aiming at an increase of methane yield in AD. For this reason, robust design resulting in efficient operation of the PST is of crucial importance for the energy balance at WWTPs. Accordingly, the improvements in the PST design should focus on the induction of a flow regime that guarantees optimal conditions for flocculation/sedimentation and hence allowing maximum PS capture rates.

2.2 Settler design

The basis for the design of sedimentation basins, or settlers, are both the suspension characteristic – particle settling characteristics, and the basin hydraulics.

2.2.1 Suspensions

Sedimentation processes are largely used in the treatment of both water and wastewaters. The different applications of this process vary accordingly with the nature and characteristics of the suspension it is meant for and the intended efficiency (Hendricks 2016).

There are four types of suspensions, distinguished by their type of settling behavior: discrete, flocculent, hindered and compression. Discrete particle suspensions, or type I suspensions, consist of particles that settle accordingly to the Stokes' law, described in Appendix A, – the fall velocity of the particles is constant. In flocculent suspensions, or Type II suspensions, the particles grow in size, increasing its velocities as they fall into the suspension. Both type I and type II suspensions have an increase in their concentration as they reach the bottom of the basement, becoming both hindered suspensions. A hindered suspension is one where the particles interact with each other. In Type IV suspensions, the particles are supported from below, and the process of sedimentation is consolidation (Hendricks 2016). Figure 3 shows the velocity of the settlement of the particles according to the type of suspension, for types I, II and III. As such, settling tanks can be categorized according to the suspension category they are designed to treat.

Primary settling, in WWTP, is considered Type II suspension settling. Type II, or flocculent suspensions, are composed of particles that tend to grow. These particles, while colliding with others, aggregate and fall at an increasing velocity, in accordance with Stokes' law (presented in Appendix A).

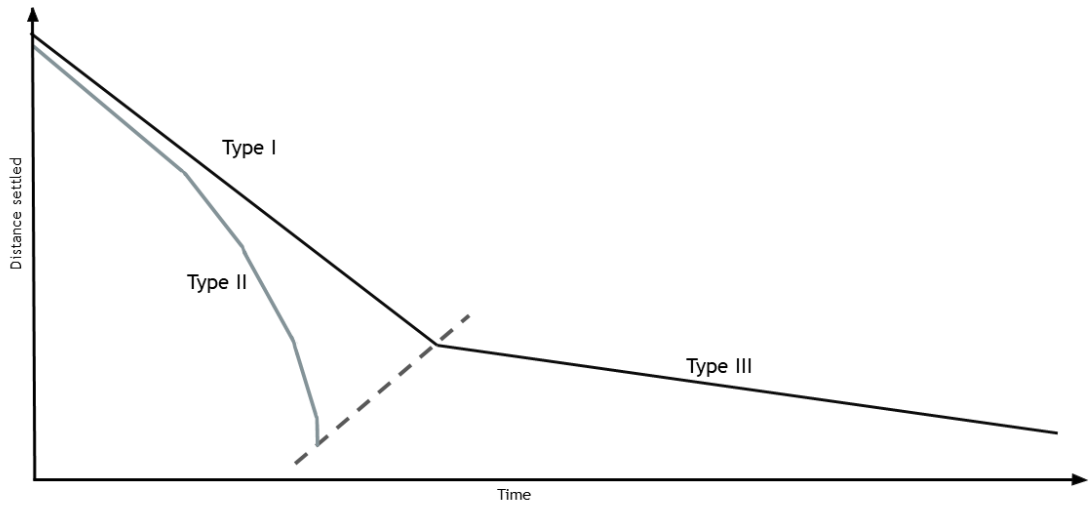

Figure 3 - Settling velocities of Suspension types I, II and III (Adapted from Hendricks (2016)).

2.2.2 Hydraulics of Settling Tanks

In an ideal settling basin, firstly theorized by Camp (1953) sedimentation occurs similarly to a motionless basin. This ideal basin has four zones as shown in Figure 4: (1) an inlet zone, where the suspension should be distributed uniformly over the cross section; (2) the settling zone, where the separation particles-liquid takes place; (3) an outlet zone for the clarified liquid, usually followed by conduct to forward the liquid and (4) an outlet zone for the sludge at the bottom of the basin.

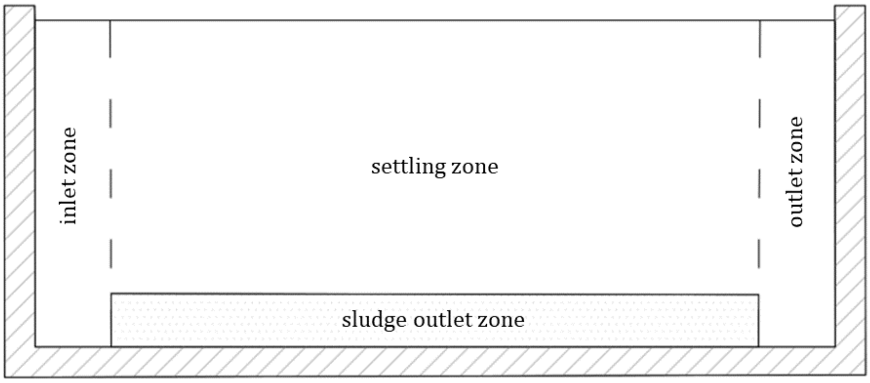

Figure 4 - Ideal Basin (Adapted from (Hendricks 2016)).

Flows are characterized by different flow patterns and circulation, having both “short circuiting” and “dead zones”. Short circuiting happens when part of the flow reaches the outlet at an exit time more quickly than the detention time whilst dead zones result from a portion of flow that leaves the settler at a time superior to the detention time. The flow patterns depend on the inlet and outlet designs, as well as the geometry and type of the settling tank (Hendricks 2016).

Settlers can be categorized according to different characteristics: the direction of flow, the shape, their location within the treatment train, the existence of plate or tube settlers or even the solids suspension or settling type (Hendricks 2016). As previously stated, the settler studied in this work is used in the primary treatment. While there are several types of PST design, in practice, the most common systems are either circular tanks with a radial flow (Figure 6a) or rectangular tanks (Figure 6b) with the horizontal (axial) flow (Hendricks 2016).

In this research work, the focus is on Circular Primary Settlers with radial flow. In circular settlers with central feed, wastewater is transported to the centre of the tank in a pipe suspended from the bridge or encased in concrete beneath the tank floor. The typical flow pattern conceptualized for these units is shown in Figure 5. In this thesis this issue will be addressed using CFD simulations, and a more accurate notion of the overall flow will be provided.

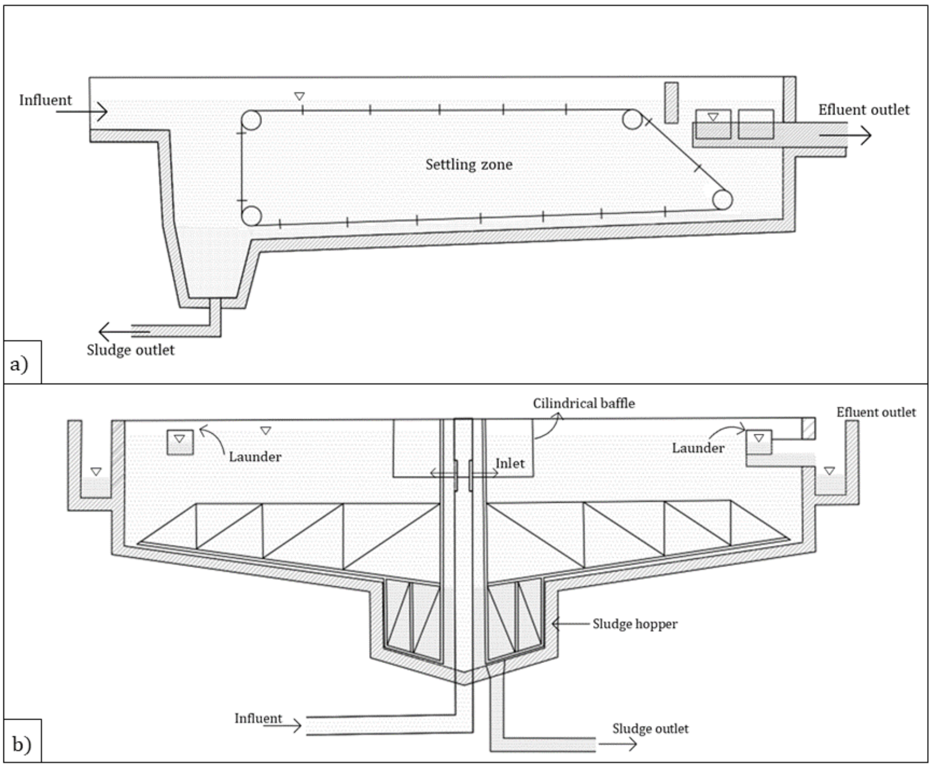

Figure 6 - Settling tank schematic: a) Rectangular; b) Circular.

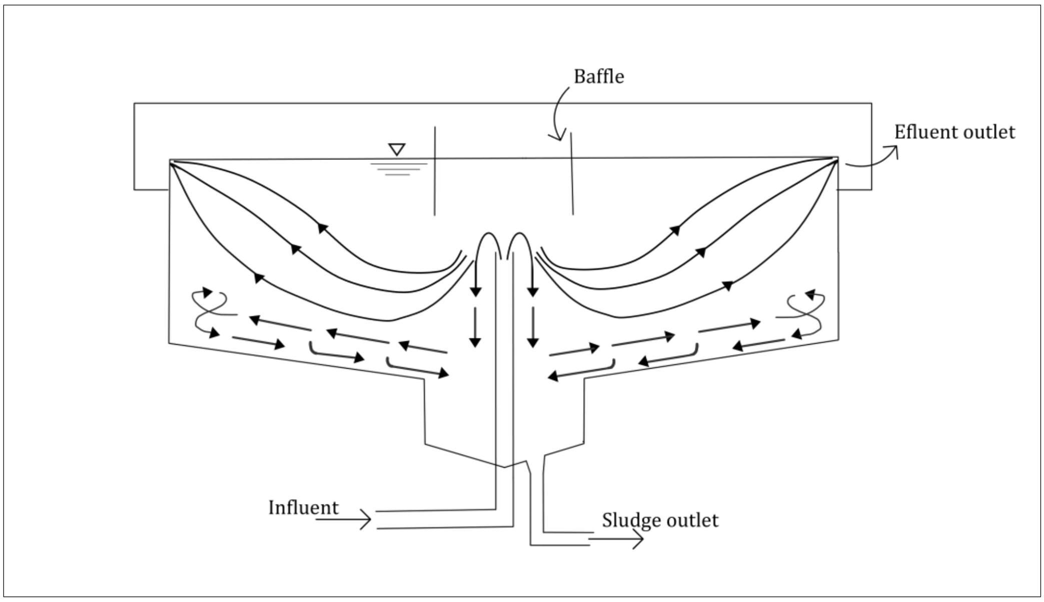

Figure 5 – Conceptualized flow patterns of a circular settler with radial flow.

As previously stated, the design of the intel region is of outmost importance for the PST's hydrodynamics. The objective of the inlet zone is to distribute the influent flow in the most efficient way to the entire cross-section area of the tank, and to create a region of turbulence to enhance particle flocculation with or without mixing a chemical agent. For that purpose, baffle devices are often used, as it is shown in Figure 5.

2.2.3 Design Guidelines for Primary Settling Tanks

Design parameters considered for circular PST's include detention time, $\theta\ (h)$, overflow rate, $v_o\ (\mathrm{m}^3/\mathrm{m}^2 \cdot d^{-1})$, horizontal velocity, $v_H\ (\mathrm{m} \cdot s^{-1})$, weir loading rate $(\mathrm{m}^3/\mathrm{m} \cdot \mathrm{d}^{-1})$, depth (m), diameter (m) and bottom slope. There is a wide variation in the recommended design parameters, as it is seen in the various guidelines existing in the technical literature. Table 1 shows a summary of these design parameters and dimensions.

Table 1 - Typical design and dimensional guidelines for circular settling tanks for WWTP - synthetized.

	Range	Typical
Detention time $[\mathrm{h}]$	1.5 – 2.5 [a]	2.0 [a]
	1.0 – 2.0 [b]	-
Overflow rate $[\mathrm{m}^3/\mathrm{m}^2 \cdot \mathrm{d}^{-1}]$	24 – 32 (average overflow rate) [a]	28 [a]
	48 – 70 (peak overflow rate) [a]	60 [a]
	< 40 [c]	-
	7 – 40 [d]	-
Weir loading rate $[\mathrm{m}^3/\mathrm{m} \cdot \mathrm{d}^{-1}]$	144 – 360 [c]	-
	125 – 500 [a]	250 [a]
Depth $[\mathrm{m}]$	3 – 4.9 [a]	4.3 [a]
	2.1 – 3.7 [b]	-
	1.0 - 5.0 [e]	2.1 [e]
Diameter $[\mathrm{m}]$	3 – 60 [a]	12 – 45 [a]
Bottom slope $[\mathrm{mm}/\mathrm{mm}]$	1/16 – 1/6 [a]	1/12 [a]

[a] Metcalf and Eddy (2014).

[b] Hendricks (2011).

[c] WPCF (1985).

[d] Camp (1953).

[e] Burns and Roe (1971).

Even though these design parameters were obtained through exhaustive empirical and mathematical studies, they lack flexibility in the adaptation to aid in the design of PSTs that help achieve recent energy and efficiency goals. The design based in these guidelines does not account for the impact of geometric and hydrodynamic parameters of the PST on the settling efficiency.

Therefore, more rigorous, and specific studies and measurements should be carried out for the conceptualization or actualization of PSTs in WWTP, for a better and more scientifically accurate designs. The empirical study of settling tanks' design parameters involves great logistics, the availability of physical tanks and the economical means to explore different designs and concepts. Computational fluid dynamics, CFD, becomes an important tool for the design of more efficient and accurate settling tanks, without the economic and time-consuming increment of physical studies. A validated CFD model is a cost-effective alternative for the evaluation of different PST design configurations and to optimize and improve performance (Xanthos et al. 2011).

2.3 Computational Fluid Dynamics applied for the design of Primary Settling Tanks

The development of Computational Simulation resources can play a significant role in the improvement of the efficiency of settling tanks' designs and impact the way these assets are studied, bringing simplicity, minimising costs and time efforts needed for complete empirical research. CFD, is a numerical tool based on the governing equations of flow and mass transfer that enables the study of flow dynamics.

Primary sedimentation tanks were one the first WWTP's units to be studied via CFD modelling due to the processes that take place in a PST: discrete, flocculent, hindered and compression settling types. Mathematical and analytical approximations have taken place to approach a simplification of PST geometries into single dimensional finite problems for the applications of CFD modelling (Samstag et al. 2016). Takamatsu et al. (1974) developed a mathematical expression for the calculation of the optimum depth of a rectangular primary settling tank through the application of radial symmetry and a floor boundary condition in his CFD model. Takamatsu et al. (1974) was one of the first researchers to approach the application of CFD for the design of PST.

Larsen (1977) a researcher and CFD pioneer, presented a work based on the study of rectangular settling tanks, and although with many simplifications, he was able to show major hydraulic phenomena related to sedimentation processes.

In the 1980's Imam (1983) was one of the firsts to apply multi-dimensional CFD models for the study of primary sedimentation, using a finite difference discretization of the governing equations to study the sedimentation of different classes of solids. Also in this decade, Abdel-Gawad and McCorquodale (1984) developed a study on nonstratified steady flow hydrodynamics of rectangular settling units using a combination of finite element methods and a strip integral method. Abdel-Gawad and McCorquodale's work emphasised the prediction of the concentration distribution and velocity fields in a PST and all their simulated results were compared and calibrated with physical tests' results that proved similar.

In the end of this decade, 1989, a 2D rectangular PST model was explored by Stamou et al. (1989) that studied the comparison between modelled solids sedimentation profiles and residence time distribution to empirical measurements.

Wang and Maxey (1993) studied the discrete settling in a flow field with homogeneous turbulence, with attention to the numerical and experimental issues. They were able to present results regarding the mean Stokes drag settling speed in uniform turbulence of zero mean velocity.

Influent wastewater presents suspensions that are highly heterogeneous with more than one sedimentation type, being the most frequent flocculant, discrete and hindered, a previously stated. Based on this, Mazzolani, Pirozzi, and d'Antonoi (1998) created a generalized settling model that includes hindered settling, to improve the model that considered only discrete particle settling. They were able to compare their results of a 2D numerical modelling simulation to models of discrete and basic hindered models, obtaining a positive outcome. In the posterior decades and until nowadays, with the advance of computational resources and fluid mathematical models, it became possible to develop more efficient and commercial CFD software (Zhang 2014).

In more recent years, CFD became a known method for the analysis of fluid flows for a wide variety of industries, but the application in wastewater and water treatments, although growing in the study of hydraulic problems, is still scarce for the analysis of physical, chemical, and biological processes. This can derivate from lack of guidance for CFD modelling (Laurent et al. 2014).

Laurent et al. (2014) proposes alternative ways to use CFD as a powerful tool to simulate integrated physical, chemical and/or biological processes in a WWTP as a means to gather information to improve unit processes designs and optimize WWTP's operations.

Griborio, McCorquodale, and Rodriguez (2014) presented a case study of the application of CFD modelling of two rectangular PST, using both 2D and 3D clarifier models and applying a Smagorinsky's type turbulence model. Griborio's study shows that the critical inputs for a PST model are compression parameters for thickened sludge and the fraction of non-settleable solids. In 2015, researchers Patziger and Kiss (2015) present a long-term research with CFD numerical modelling and in situ tests of a rectangular PST, analysing the suspended solids transport processes. Patziger's work presented a 2D numerical model of the rectangular PST, considering all important physical processes (inhomogeneous turbulent flow, mass transport and settling) with a $k - \varepsilon$ turbulence model. In this paper it was concluded that the density effects in the inlet zone can be neglected, but that this location presents high velocity components that affect the efficiency of the PSTs operation, leading to large recirculation and dead zones.

Wicklein et al. (2015) published an article that summarizes the good modelling practices, in the application of CFD to WWTP and water treatment cases. This study considers that the potential of CFD in WWTP studies is not being explored in the fullest, due to the lack of training of the practitioners of CFD modelling and lack of guidance, presenting an article regarding good methods and practices for a better use of CFD in these applications. Some of these tips and guidance were taken in consideration in this work.

Even though it exists, current literature on PST design with CFD is still scarce and limited to the reduced number of works referenced above. PST can have a key role on increasing nutrient removal and reducing energy consumption in a WWTP. These are major goals in the modern operation of WWTPs. Technological enhancements in these well-established organs are only possible by introducing more advanced design tools. This work addresses this challenge by assessing CFD models for the circular PST, which is the workhorse of primary treatment in modern WWTPs, and by introducing methods to qualify the performance of simulated PSTs.

3 2D CFD Modelling of a Primary Settler

The preparation of this work's CFD model concerned the geometry domain and boundary conditions assessment. It was also necessary to choose the models best suited to the study of the intended geometry domain's flow and particle settling behavior as well as the programming and schematization of the tests and simulations.

3.1 Physical Domain

The geometry addressed in this chapter is a cross section of a circular primary settler. This 2D surface, corresponds to half of this cross section that when rotated around its axis creates the entirety of the circular settler.

The flow in a circular settler is reported in this section using the finite volume software package Ansys Fluent 2022 R1. The respective necessary mesh and geometry were built in Design Modeler and Meshing available in Ansys Workbench 2022 R1.

A 2D sketch of the circular settler is shown in Figure 7. This geometry corresponds to the entire cross section of a primary circular settler, and it is based in a primary settler of a wastewater treatment plant from the South Coast of England. However, the simulations were performed using a simplification of the geometry, an axisymmetric domain, shown in Figure 8. The CFD domain is described in Table 2.

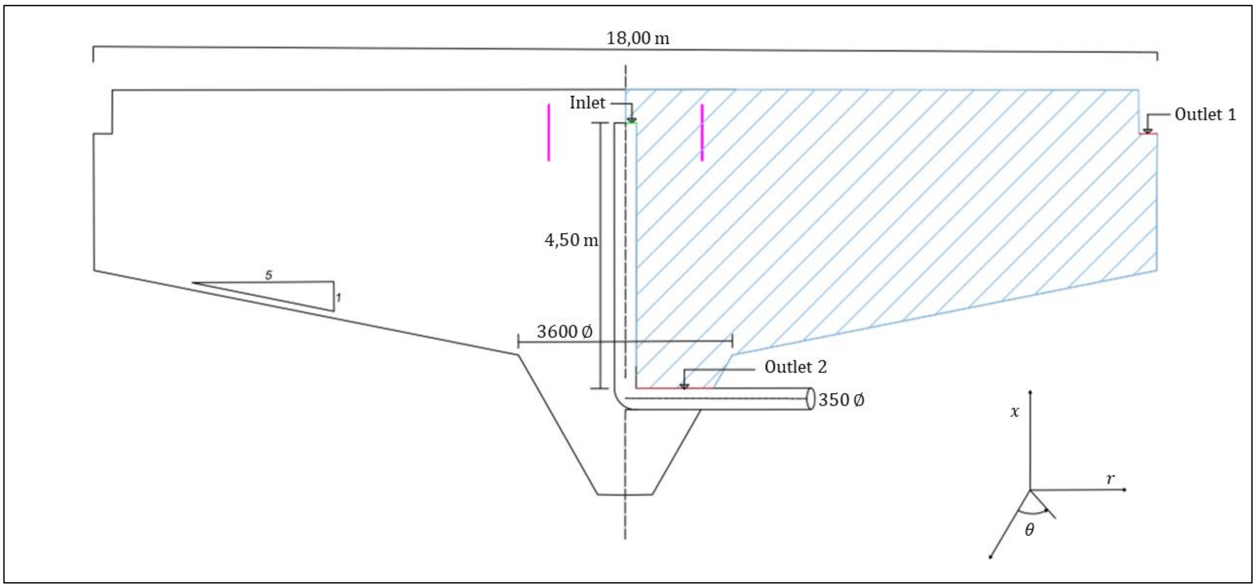

Figure 7 - Circular Primary Settler cross section.

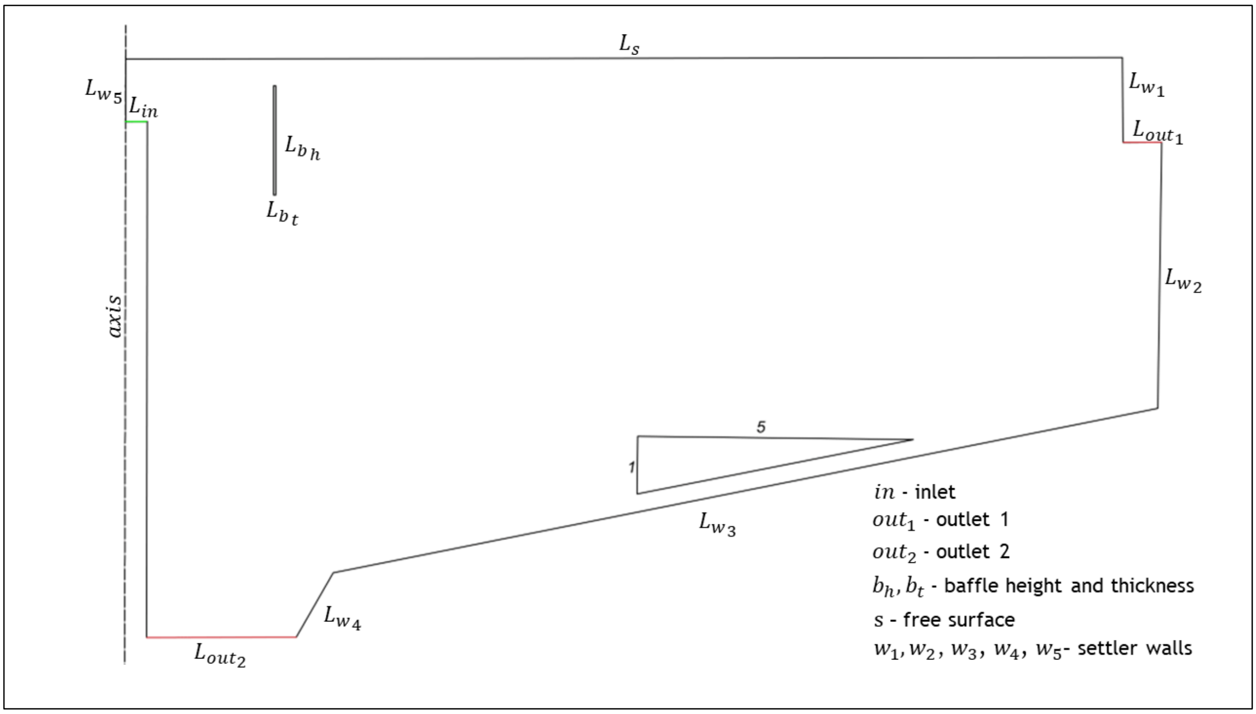

Figure 8 – Axisymmetric 2D CFD geometric domain.

Table 2 - Measurements of the geometry domain.

L_{in}	0.175 m	L_{W_1}	0.55 m	L_s	9.00 m
L_{out_1}	0.30 m	L_{W_2}	2.05 m	L_{b_h}	0.95 m
L_{out_2}	1.80 m	L_{W_3}	7.33 m	L_{b_t}	0.20 m

The simulated primary settler has a total diameter of 18.0 m, a surface area of 254 m^2. This primary settler is one of 2 duty PST units at the WWTP serving a population equivalent of 37 410 habitants.

In this work, the influence of the baffle's location on the flow is studied. Therefore, the distance from the baffle to the axis ($axis$ in Figure 8) and to the surface (s in Figure 8) is a variable under study in this section.

3.2 Governing equations and boundary conditions

In ANSYS Fluent 2022 R1, the flow simulations are based on the conservation laws of physics, i. e. the mass conservation principle and the momentum conservation (Newton's Second Law). These principles are applied through governing equations (Ansys 2022).

Considering steady-state, incompressible fluids and neglecting body forces, the mass conservation equation in cylindrical coordinates (see Figure 7) for axisymmetric cases is given by,

$$\frac{\partial \rho}{\partial t}+\frac{\partial}{\partial x}(\rho v_x)+\frac{\partial}{\partial r}(\rho v_r)+\frac{\rho v_r}{r}=0 \tag{1}$$

where, ρ is the density, v_x is the axial velocity, v_r is the radial velocity and r is the radial coordinate.

For the case of steady-state 2D axisymmetric simulations, the axial and radial momentum conservation equations are expressed respectively by,

Axial momentum

$$\frac{1}{r}\frac{\partial}{\partial x}(r\rho v_x v_x)+\frac{1}{r}\frac{\partial}{\partial r}(r\rho v_r v_x) = -\frac{\partial p}{\partial r}+\frac{1}{r}\frac{\partial}{\partial x}\left[r\mu\left(2\frac{\partial v_x}{\partial x}\right)\right]+\frac{1}{r}\frac{\partial}{\partial r}\left[r\mu\left(\frac{\partial v_x}{\partial r}+\frac{\partial v_r}{\partial x}\right)\right] \tag{2}$$

Radial momentum

$$\frac{1}{r}\frac{\partial}{\partial x}(r\rho v_x v_r)+\frac{1}{r}\frac{\partial}{\partial r}(r\rho v_r v_r) = -\frac{\partial p}{\partial r}+\frac{1}{r}\frac{\partial}{\partial x}\left[r\mu\left(\frac{\partial v_r}{\partial x}+\frac{\partial v_x}{\partial r}\right)\right]+\frac{1}{r}\frac{\partial}{\partial r}\left[r\mu\left(2\frac{\partial v_r}{\partial r}\right)\right]-2\mu\frac{v_r}{r^2} \tag{3}$$

where, for incompressible flow,

$$\nabla\cdot\vec{v}=\frac{\partial v_x}{\partial x}+\frac{\partial v_r}{\partial r}+\frac{v_r}{r}=0 \tag{4}$$

In this work, the working fluid is water, at temperature of 20ºC ($\rho = 998.2\ \mathrm{kg\,m^{-3}}$; $\mu = 0.001\ \mathrm{kg\,m^{-1}\,s^{-1}}$). For a steady flow, the partial time derivatives are zero.

The boundary conditions imposed to the simulation were the inlet velocity (in in Figure 8) using the expression,

$$v_r = u_c\,(1-\frac{r}{R})^{\frac{1}{\mathrm{n}}} \tag{5}$$

with,

$$\mathrm{n} = 0{,}462\log(\mathrm{Re})^2 - 3{,}24\log(\mathrm{Re}) + 11{,}6 \tag{6}$$

where u_c is the influent velocity of the liquid in m s^{-1}, R, is the radius of the inlet pipe, and Re is the inlet Reynolds number defined as,

$$\mathrm{Re} = \frac{v\,\rho\,D}{\mu} \tag{7}$$

For the inlet, it was also set the Turbulent Intensity, I_t, which is given by the following expression,

$$I_t = 0{,}16\, Re^{-\frac{1}{8}} \tag{8}$$

Regarding the free surface (s), it was imposed a specified shear of 0 Pa. The boundary condition for the $axis$ was defined as axis for the simulation of axisymmetric geometry.

Outflow boundary conditions were set at the two outlets. The fractions of outflow in each outlet are 0.995 for outlet 1 (out_1 in Figure 8) and 0.005 for outlet2 (out_2 in Figure 8).

3.2.1 Turbulence Model – The K-εTurbulence Model

The conditions studied in this work required setting a turbulent model due to the conditions imposed at the inlet. According to the flow hydraulics, the RNG (Renormalization Group theory) k-ε model was the chosen model. This model is similar to the Standard k-ε model.

For turbulent flow, the 2D axisymmetric Navier-Stokes equations were averaged using the decomposition of the velocity components in an average, $\overline{v_i}$, and a fluctuating component, v'_j, which translate into: $v_i = \overline{v_i} + v'_j$. The Reynolds Averaged Navier-Stokes equations for the 2D axisymmetric take the form:

Axial Momentum

$$\frac{1}{r}\frac{\partial}{\partial x}(r\rho\overline{v_x}\overline{v_x}) + \frac{1}{r}\frac{\partial}{\partial r}(r\rho\overline{v_r}\overline{v_x}) = -\frac{\partial p}{\partial r} + \frac{1}{r}\frac{\partial}{\partial x}\left[2r\mu\frac{\partial\overline{v_x}}{\partial x} - \rho r\overline{(v'_r)^2}\right] + \frac{1}{r}\frac{\partial}{\partial r}\left[r\mu\left(\frac{\partial\overline{v_x}}{\partial r} + \frac{\partial\overline{v_r}}{\partial x}\right) - \rho r\overline{v'_r v'_x}\right] \tag{9}$$

Radial Momentum

$$\frac{1}{r}\frac{\partial}{\partial x}(r\rho\overline{v_x}\overline{v_r}) + \frac{1}{r}\frac{\partial}{\partial r}(r\rho\overline{v_r}\overline{v_r}) = -\frac{\partial p}{\partial r} + \frac{1}{r}\frac{\partial}{\partial x}\left[r\mu\left(\frac{\partial\overline{v_r}}{\partial x} + \frac{\partial\overline{v_x}}{\partial r}\right) - \rho r\overline{v'_r v'_x}\right] + \frac{1}{r}\frac{\partial}{\partial r}\left[2r\mu\frac{\partial\overline{v_r}}{\partial r} - \rho r\overline{(v'_x)^2}\right] - 2\mu\frac{v_r}{r^2} \tag{10}$$

These equations have new unclosed terms, the Reynolds stresses: $(v'_r)^2$, $(v'_x)^2$, and $\overline{v'_r v'_x}$, that are modeled from the turbulent viscosity μ_t, and the turbulent kinetic energy, k, as

$$-\rho\overline{(v'_r)^2} = 2\mu_t\frac{\partial v_r}{\partial r} - \frac{2}{3}\rho k \tag{11}$$

$$-\rho\overline{(v'_x)^2} = 2\mu_t\frac{\partial\overline{v_x}}{\partial x} - \frac{2}{3}\rho k \tag{12}$$

$$-\rho\overline{v'_r v'_x} = \mu_t\left(\frac{\partial\overline{v_r}}{\partial x} + \frac{\partial\overline{v_x}}{\partial r}\right) \tag{13}$$

In RANS equation, turbulence terms, such as Reynolds stresses, are unclosed. The unclosed turbulent terms must be modeled. The RNG model is based on model transport equations for the turbulent kinetic energy, k, the turbulent energy dissipation, ε and on the turbulent (or eddy) viscosity.

The expression for the kinetic energy is given by,

$$\frac{\partial}{\partial t}(\rho k) + \frac{\partial}{\partial x_i}(\rho k v_i) = \frac{\partial}{\partial x_j}\left[\alpha_k \mu_{eff} \frac{\partial k}{\partial x_j}\right] + G_k + G_b + \rho\varepsilon - Y_M + S_k \tag{14}$$

the rate of energy dissipation is expressed by,

$$\frac{\partial}{\partial t}(\rho \varepsilon) + \frac{\partial}{\partial x_i}(\rho \varepsilon v_i) = \frac{\partial}{\partial x_j}\left[\alpha_\varepsilon \mu_{eff} \frac{\partial \varepsilon}{\partial x_j}\right] + C_{1\varepsilon}\frac{\varepsilon}{k}(G_k + C_{3\varepsilon}G_b) - C_2\rho\frac{\varepsilon^2}{k} - R_\varepsilon + S_\varepsilon \tag{15}$$

where G_k is the generation of turbulence kinetic energy due to the mean velocity gradients, G_b is the generation of turbulence kinetic energy from buoyancy, Y_M is the contribution of the fluctuating dilatation in compressible turbulence to the overall dissipation rate. s_k and s_ε are user-defined source terms, which are not used in this work. α_k and α_ε are respectively the inverse effective Prandlt numbers for k and ε and finally $C_{1\varepsilon}$, $C_{2\varepsilon}$, $C_{3\varepsilon}$ and C_μ are constants. The constants $C_{1\varepsilon}$ and $C_{2\varepsilon}$, present in Equation 15 have default values of 1.42 and 1.68 respectively.

The scale elimination procedure in RNG calculations results in a differential equation for turbulent viscosity, as follows,

$$d\left(\frac{\rho^2 k}{\sqrt{\varepsilon\mu}}\right) = 1.72\,\frac{\hat{v}}{\sqrt{\hat{v}^3 - 1 + C_v}}\,d\hat{v} \tag{16}$$

where $C_v \approx 100$, and

$$\hat{v} = \frac{\mu_{eff}}{\mu} \tag{17}$$

Equation 16 is integrated to better describe how turbulent transport's effectiveness varies with the Reynolds number and to better adapt to low-Reynolds numbers and near-wall flows.

In ANSYS Fluent, the turbulent viscosity is computed using the following expression,

$$\mu_t = \rho C_\mu \frac{k^2}{\varepsilon} \tag{18}$$

where $C_\mu = 0.0845$.

The term R_ε in Equation 9 is an additional term when compared to the equations used by the Standard k-ε model, and is given by

$$R_\varepsilon = \frac{C_\mu \rho \eta^3 (1 - \eta/\eta_0)\varepsilon^2}{1 + \beta\eta^3} \tag{19}$$

where $\eta \equiv Sk/\varepsilon$, $\eta_0 = 4.38$, $\beta = 0.012$, and S is the entropy.

3.3 Numerical Solution – steady state

CFD simulations were set at steady state, i.e., the transient terms are zero and water was set as working fluid. For these simulations, it was used the Coupled scheme for the pressure-velocity coupling; for the spatial discretization, it was used Second order for the pressure and Second order upwind for both turbulent kinetic energy and turbulent dissipation rate. The convergence criteria of the simulations were the residuals of 10^{-4}.

3.4 Grid Independence Test

The grid independence test is crucial to minimize the computing resources and time for simulation, while checking numerically the validity of the CFD model. For the mesh validation, the geometry is drawn according to Figure 8 and 5 element sizes were studied. Table 3 shows the element size, the number of elements and the average skewness for each mesh. The parameters for grid independence test were the streamlines arrangement in the flow domain, the Turbulent Kinetic Energy distribution, the Turbulence Energy Dissipation and the Y^* on the wall.

The meshes were generated using the Automatic Method (Quadrilateral Dominant), with inflation on the walls w_1, w_2, w_3, w_4, w_5, b_h and b_t (from Figure 8) and with edge sizing with a bias factor of 10 in the inlet (in in Figure 8).

The methods to generate the mesh were kept for the five cases. Only the element size was changed. Thus, the average skewness is kept constant. The mesh is quite regular, isotropic and so the skewness is close to 0.9.

Table 3 - Element sizes and number of elements for the studied.

	Mesh				
	Mesh0175	Mesh015	Mesh012	Mesh010	Mesh008
Element size [m]	0.0175	0.015	0.012	0.010	0.008
Number of elements	126 159	163 531	252 584	360 342	539 854
Average Skewness	0.87	0.89	0.91	0.91	0.91

Figure 9, Figure 10 and Figure 11 show the streamlines in the settling tank, the Turbulence Dissipation Rate, ε, and the Turbulent Kinetic energy, k, respectively. These maps will be used to assess the independence of the flow results from the mesh.

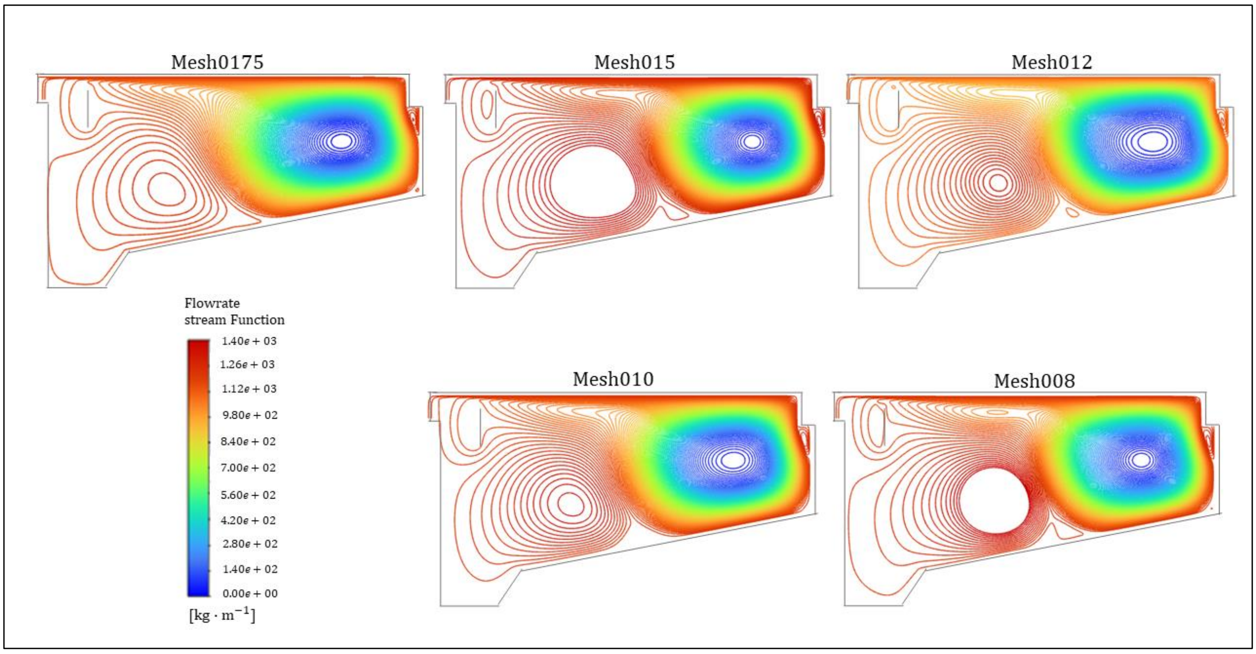

Figure 9 – Flowrate Streamlines of meshes 0175, 015, 012, 010 and 008.

Figure 9 shows that there are two large vortices, that promote the recirculation in the settler. The configuration of these vortices is unstable, and so its geometry is quite dependent on the simulation's conditions. Nevertheless, the vortices structure's location and average size shows slight dependence on the mesh. So, the mesh assessment will be based on variables related to the overall turbulence distribution.

For the contour maps of Turbulent Energy Dissipation and Turbulent Kinetic Energy, the five meshes do not present differences between them. The turbulent kinetic energy is concentrated in the path of the inlet's flow stream, being dissipated with the radial spreading of the flow. This region also coincides with the regions of largest turbulent energy dissipation. The overall distribution of both variables is remarkably similar for the five meshes tested.

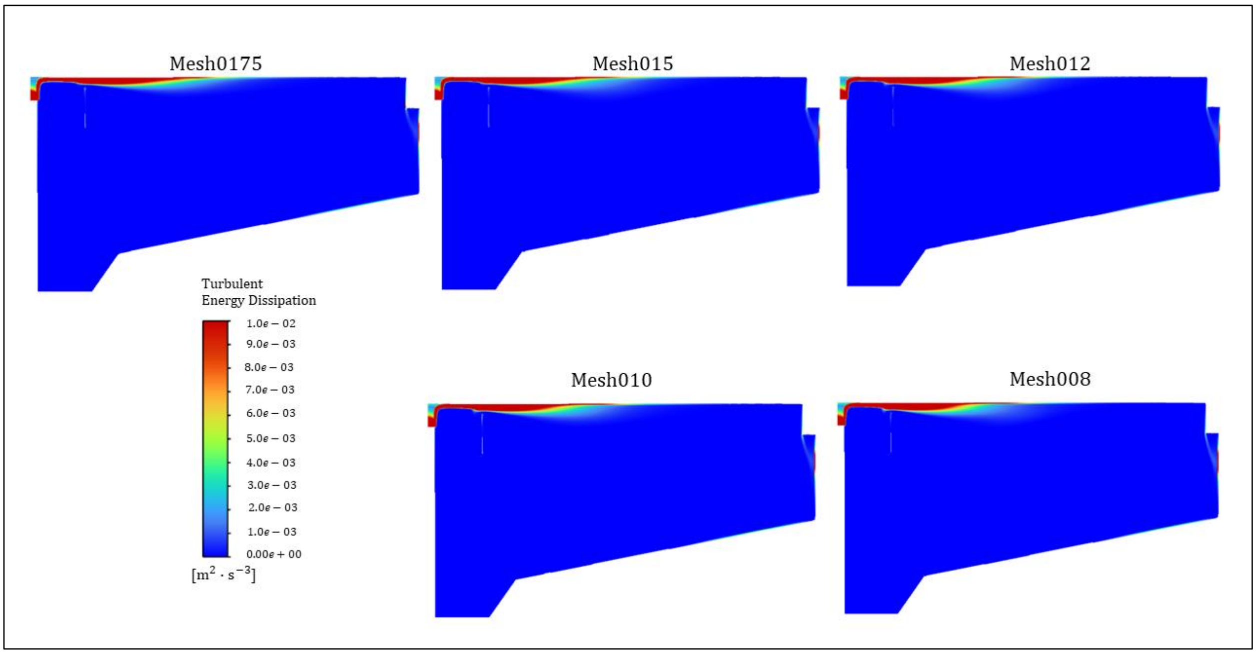

Figure 10 - Turbulent Energy dissipation on the inlet of meshes 0175, 015, 012, 010 and 008.

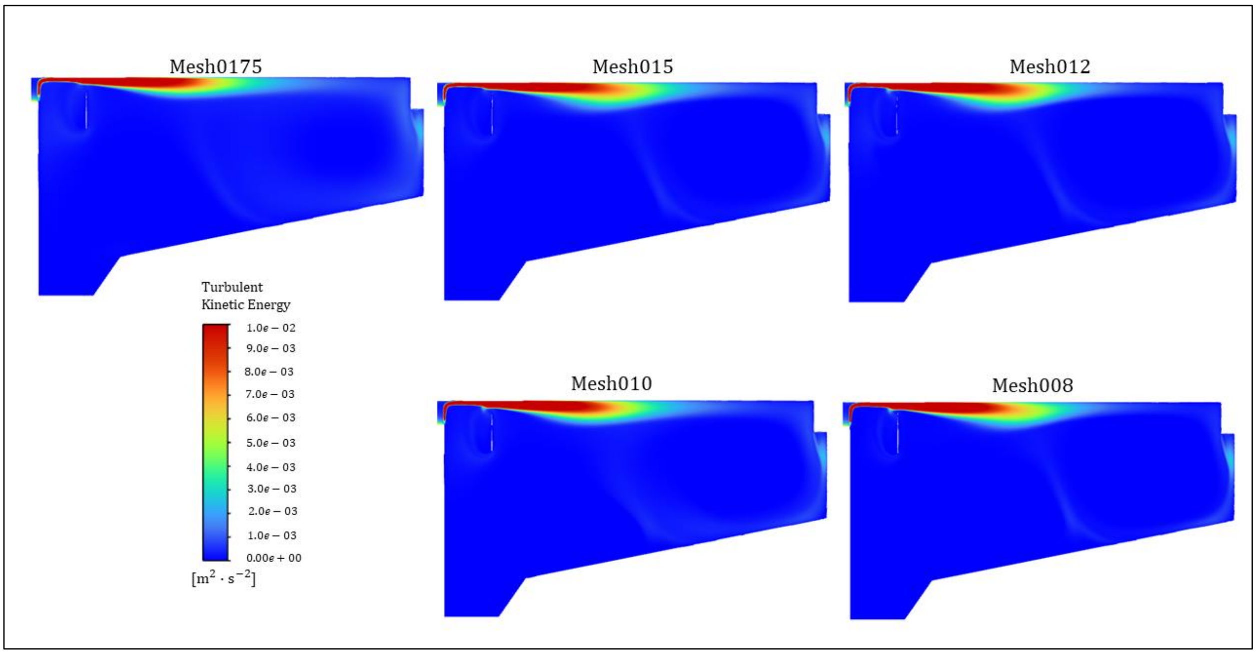

Figure 11 - Turbulent Kinetic Energy on the inlet of meshes 0175, 015, 012, 010 and 008.

For a more sensitive analysis of meshes, a cross section line (cross section line 1 in Figure 12) of the geometric domain was drawn to obtain the variation of k and ε with the tank depth, for each mesh. The cross-section line 1 is situated at 7.50 m from the axis and crosses the vortex created on the right side of the geometric tank surface. This line is shown in Figure 12 and

Figure 13. For the verification of the chosen wall functions – Scalable wall functions, the values of the parameter Y^*(Y star) were also obtain from cross section line 1, as reported in Table 4.

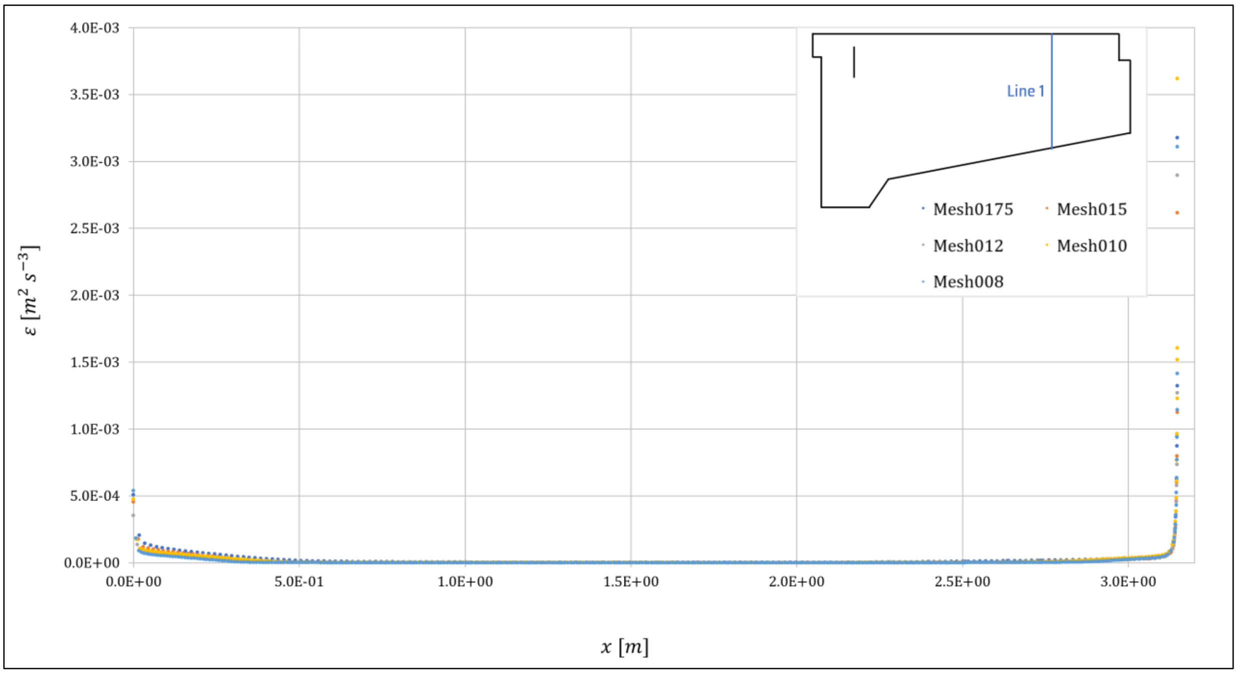

Figure 12 - Turbulent Energy Dissipation at cross section line 1.

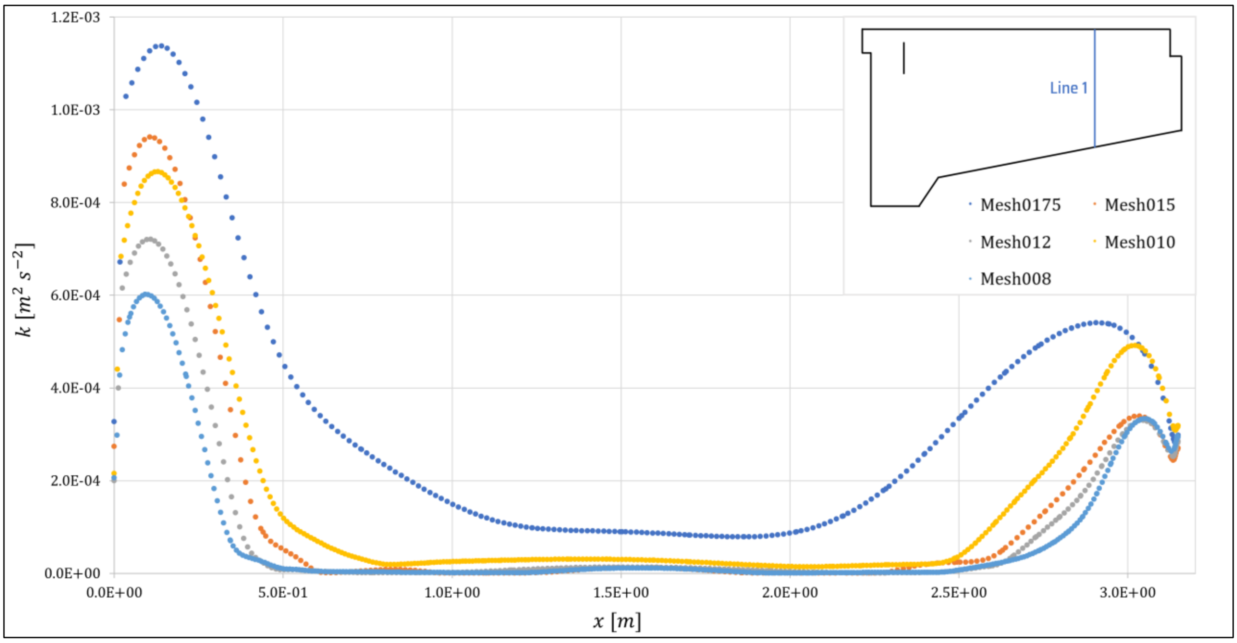

Figure 13 - Turbulent Kinetic Energy at cross section line 1.

Table 4 - Wall Y^* for the 5 tested meshes.

	Y^*				
x [m]	Mesh0175	Mesh015	Mesh012	Mesh010	Mesh008
3.15	11.23	11.23	11.23	11.23	11.23

All the tested meshes present an $Y^* > 11$, so the application of scalable wall functions for the simulation is verified. On the plot of the turbulent energy dissipation Figure 12, all meshes have the same profile. Regarding the variation of turbulent kinetic energy in line 1 (Figure 13), it is possible to conclude that the profiles for all the meshes follow a similar profile, with meshes Mesh0175 and Mesh010 slightly deviating from the pattern. The differences between flow patterns, where the position of the streamlines is unstable, are the underlying reason for the fact that there is not a well-defined evolution of the turbulent kinetic energy profiles with the mesh size. All three remaining meshes, Mesh015, Mesh012 and Mesh008 are in agreement to each other; therefore, Mesh012 was chosen because it has enough elements to simulate the flow and uses fewer computational resources comparing to Mesh008. In Figure 14, Mesh012 and some of its detailed zones are shown, where it is possible to observe: the cell geometry, the inflation of the walls and the edge sizing in the inlet (Figure 14a). From the independence test, it became adequate to proceed to the design studies described in the following sections.

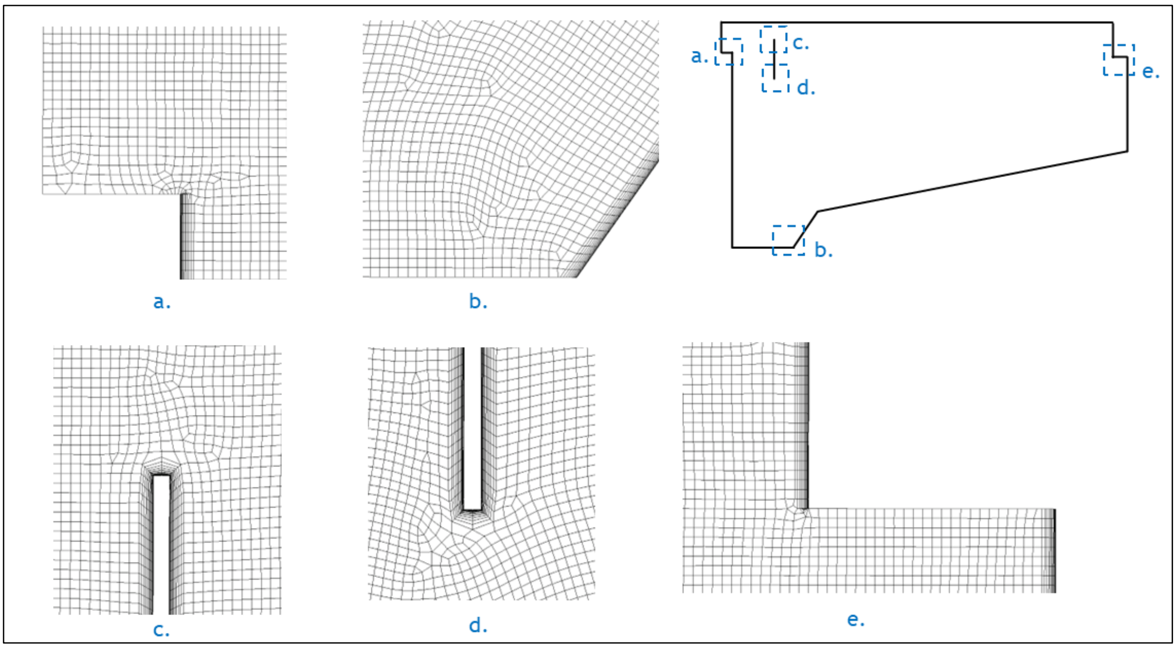

Figure 14 - Mesh012 details.

3.5 CFD Simulations of different Inlet designs

For the first part of this work's simulation plan, CFD simulations were performed according to the models described in sections 3.1 through 3.3 and using Mesh012 with different inlet designs PST case study. The dimensions and designs of 5 different inlets are shown in Figure 15. In this work, both velocities, υ_1 and υ_2 were tested, so 10 tests were carried out in total as shown in Table 5.

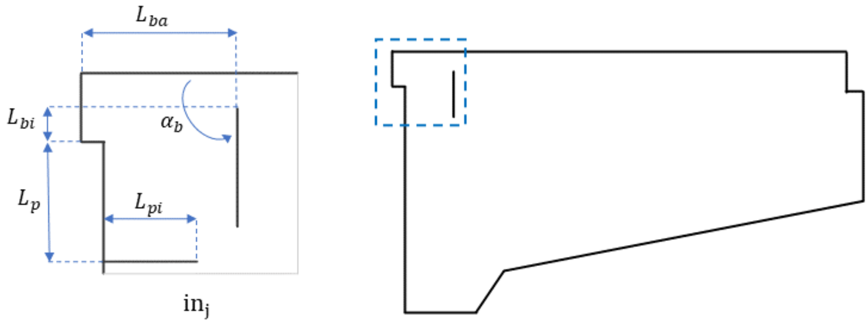

	L_{ba} [m]	L_{bi} [m]	L_p [m]	L_{pi} [m]	α_b
$\mathrm{in_1}$	1.30	0.30	-	-	90°
$\mathrm{in_2}$	1.30	0.10	-	-	90°
$\mathrm{in_3}$	1.30	0.50	-	-	90°
$\mathrm{in_4}$	1.30	0.50	0.50	0.50	90°
$\mathrm{in_5}$	1.30	0.30	-	-	70°

Figure 15 - Inlet design and measurements for the hydraulic simulations.

Table 5 - Planification and identification of simulations.

	Influent velocity υ_c [m s^{-1}]	
$\mathrm{in_j}$	$\upsilon_1 = 2.2$	$\upsilon_2 = 1.0$
$\mathrm{in_1}$	$\mathrm{in_1}\upsilon_1$	$\mathrm{in_1}\upsilon_2$
$\mathrm{in_2}$	$\mathrm{in_2}\upsilon_1$	$\mathrm{in_2}\upsilon_2$
$\mathrm{in_3}$	$\mathrm{in_3}\upsilon_1$	$\mathrm{in_3}\upsilon_2$
$\mathrm{in_4}$	$\mathrm{in_4}\upsilon_1$	$\mathrm{in_4}\upsilon_2$
$\mathrm{in_5}$	$\mathrm{in_5}\upsilon_1$	$\mathrm{in_5}\upsilon_2$

3.6 Sedimentation of discrete particles using DPM

For the second part of this work, six simulations were carried out with a Discrete Phase Model, DPM, to simulate discrete particles in the PST case study. Ansys Fluent 2022 R1 follows the Euler-Lagrange approach for multiphase simulations. In this case, water is the fluid phase and discrete particles correspond to the dispersed phase. The disperse phase is solved by tracking a large number of particles through the flow field previously calculated. In this case, the flow field used for this study was the one calculated for the conditions $\mathrm{in}_1\upsilon_1$ (Table 5).

The transient state was set in CFD simulations for the DPM, and particle-particle interactions were neglected. The particles trajectory was computed individually at adaptative time-steps, with a minimum of 0.001 s and a maximum of 1 s.

Ansys Fluent commercial package determines the trajectory of a discrete particle by integrating the force balance acting on the particle, which is written in a Lagrangian reference frame, and equalised to the particle's inertia with the forces acting on the particle, according to,

$$m_p \frac{d\overrightarrow{v_p}}{dt} = m_p \frac{\vec{v} - \overrightarrow{v_p}}{\tau_r} + m_p \frac{\vec{g}(\rho_p - \rho_f)}{\rho_p} + \vec{F} \quad (16)$$

where m_p is the particle mass, $\vec{v}$ is the fluid velocity, $\overrightarrow{v_p}$ is the particle velocity, ρ_f is the fluid's specific mass, or density, ρ_p is the particle's specific mass, $\vec{F}$ is an additional force, $m_p \frac{\vec{v}-\overrightarrow{v_p}}{\tau_r}$ is the drag force, and τ_r is the particle's relaxation time, calculated through,

$$\tau_r = \frac{\rho_s D_s^2}{18\mu} \frac{24}{C_D \mathrm{Re_r}} \quad (17)$$

where D_s is the particle diameter and $\mathrm{Re_r}$ is the relative Reynolds number, defined as

$$\mathrm{Re_r} = \frac{\rho D_s |\overrightarrow{v_p} - \vec{v}|}{\mu} \quad (18)$$

For DPM simulations, the particles rotation was neglected as well as the additional forces, $\vec{F}$.

The simulated flow that is the initial condition for DPM simulations was a turbulent flow simulation. When the flow is turbulent, Ansys Fluent predicts the trajectory of particles using the mean fluid velocity, $\bar{v}$, in the trajectory in Equation 16.

Six injections of 1000 discreate particles, ϕ_i, simulated separately. All the particles were injected at the inlet, and the chosen material properties for the particles are from Anthracite ($\rho_A = 1200\ \mathrm{kg\ m^{-3}}$) with six different diameters, to better simulate influent particle's behaviour. Each particle injection was simulated with the highest influent velocity $v_1 = 2.2\ \mathrm{m\ s^{-1}}$ which corresponds to the peak flow provided by a WWTP of the South Cost of England. The simulation plan is shown in Table 6.

Table 6 - DPM simulations plan and respective working conditions.

ϕ_i	Particle diameter [m]
ϕ_1	1.0×10^{-5}
ϕ_2	2.0×10^{-5}
ϕ_3	4.0×10^{-5}
ϕ_4	1.0×10^{-4}
ϕ_5	2.0×10^{-4}
ϕ_6	1.0×10^{-3}

4 Results and discussion

The present chapter addresses the results obtained for the simulations described in sections 3.5 and 3.6, for the inlet variation simulations and the DPM simulations respectively. This chapter also presents a Settling Expedite Assessment Method developed during this thesis which predicts the particle settling using only the particle's terminal velocity and CFD simulation of a flow.

4.1 Results of CFD Simulation for the inlet designs

For each simulation $\mathrm{in_j}\upsilon_c$ flowrate streamlines were plotted to analyze the flow in the tank and to choose the strategic locations to register turbulent energy dissipation, ε, turbulent kinetic energy, k, and velocity, υ. The flowrate streamlines show two large vortices, vortex 1 on the right and vortex 2 on the left, where two cross section lines were created, using CFD Post in Ansys Workbench 2022 R1. Figure 16 shows the locations of lines used to report data in these sections, namely the cross-sections lines (Line 1 and 2) and the surface line. Line 2 (Figure 16) enables the identification of vortex 2, whose location is largely influenced by the inlet design. Line 1 crosses vortex 1, that presents itself in the same location for every simulation. Therefor the position of line 2 is changing according to the position of the center of vortex 2. Shows the streamlines for each condition and the respective position of lines 1 and 2.

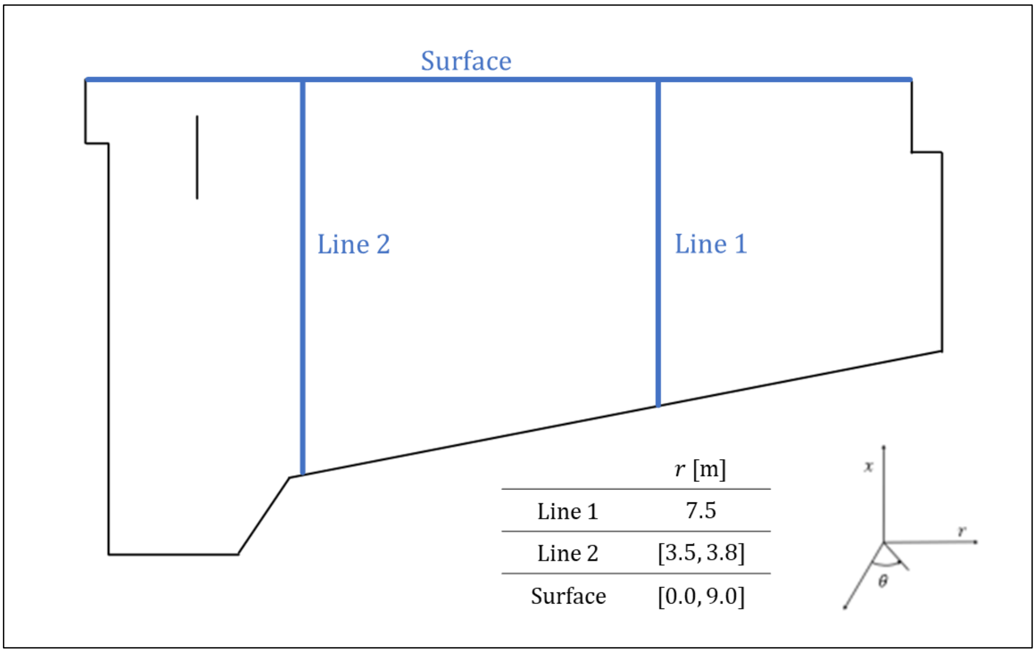

	r [m]
Line 1	7.5
Line 2	[3.5, 3.8]
Surface	[0.0, 9.0]

Figure 16 - Cross-section lines for data collection of inlet design variation results.

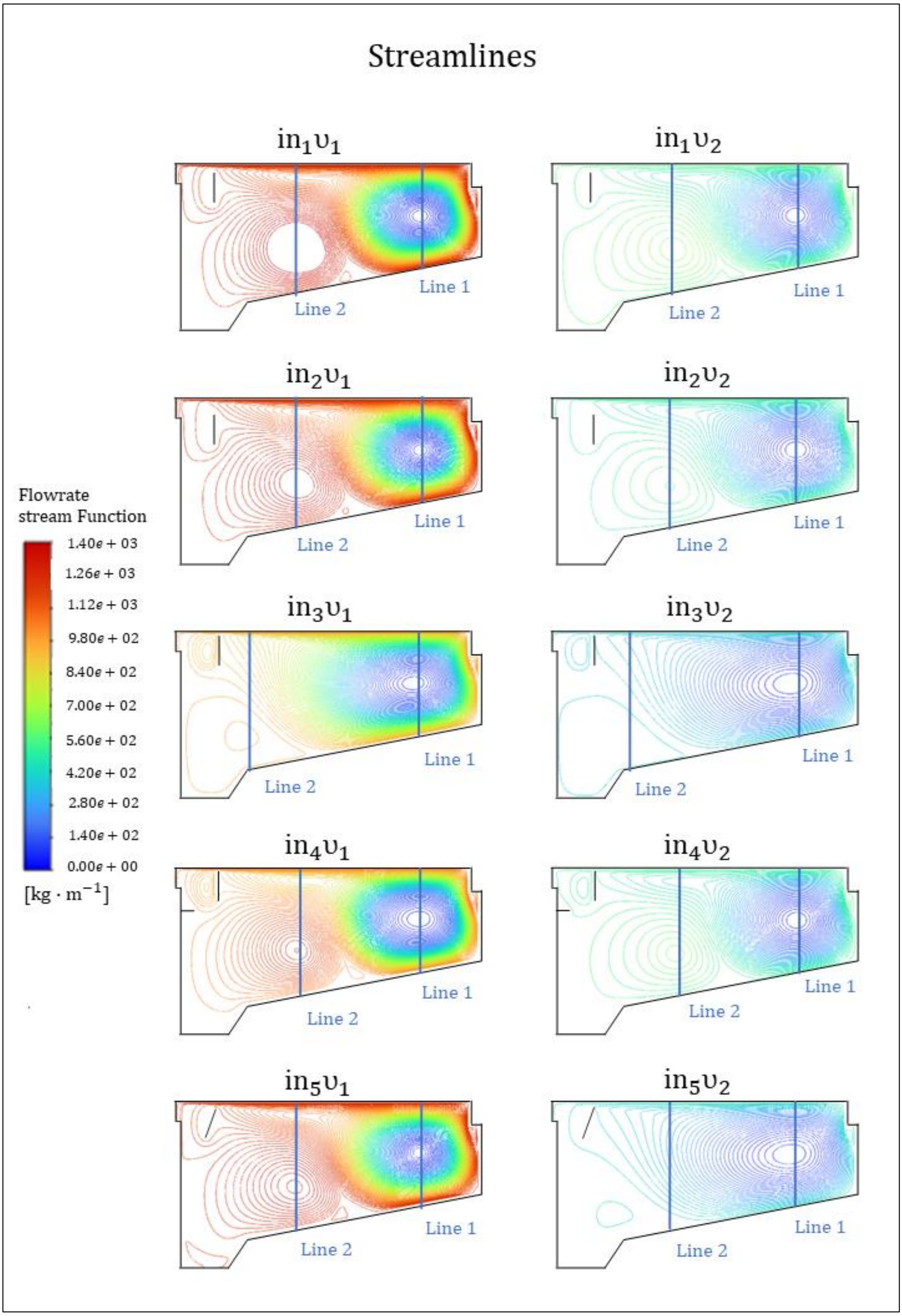

Figure 17 - Streamlines and cross line positions for simulations $in_j \upsilon_c$.

The streamlines show that the main features of the flow in the PST are set from the clearance above the ring baffle. A jet issues from the gap above the ring, creating a shortcut from inlet to outlet. This jet induces the two large circulation regions, i.e., the two vortices located in the middle of the PST. These vortices are unstable and, make the flow very sensible to boundary conditions and numerical parameters as reported from the meshing studies.

In the first geometry, simulations $\mathrm{in}_1\upsilon_1$ and $\mathrm{in}_1\upsilon_2$, the jet issuing over the ring baffle promotes a circulation region clearly divided into two vortices. The left one (vortex 2) is centred at deeper regions of the PST and does not contact directly with the inlet jet. The one on the right (vortex 1), further downstream in the PST, covers the complete length of the jet with a well-defined roundish circulation region, close to the outlet; and a squeezed region closer to the ring baffle located above vortex 2. The same flow patterns are observed for the two velocity values, υ_1 and υ_2, and for the larger gap space over the ring, in_2 (simulations $\mathrm{in}_2\upsilon_1$ and $\mathrm{in}_2\upsilon_2$). For the smaller gap simulations, $\mathrm{in}_3\upsilon_1$ and $\mathrm{in}_3\upsilon_2$, a narrower faster jet issues above the ring, pushing the vortex 2 to the bottom of the PST, making the overall flow dominated by vortex 2. The same flow pattern is observed for the two simulated velocities. The alteration of the vortices position for conditions $\mathrm{in}_3\upsilon_1$ and $\mathrm{in}_3\upsilon_2$ shows further the unstable nature of these structures.

For conditions $\mathrm{in}_4\upsilon_1$ and $\mathrm{in}_4\upsilon_2$, the ring baffle is placed in the region bellow the ring baffle. There is a small vortex formed in the inlet region that interplays with vortex 2. The disk baffle interferes with the flow circulation in this region. Although the gap is the same as for $\mathrm{in}_3\upsilon_1$ and $\mathrm{in}_3\upsilon_2$, the overall recirculation patterns of the large vortices are similar for the conditions $\mathrm{in}_1\upsilon_1$, $\mathrm{in}_1\upsilon_2$, $\mathrm{in}_2\upsilon_1$ and $\mathrm{in}_2\upsilon_2$.

The last configuration was a tilted ring baffle. Condition $\mathrm{in}_4\upsilon_1$ exhibited the same flow patterns as simulations as $\mathrm{in}_1\upsilon_1$ and $\mathrm{in}_1\upsilon_2$. But for the lower velocity, condition $\mathrm{in}_4\upsilon_2$, the flow patterns were the same as in $\mathrm{in}_3\upsilon_1$ and $\mathrm{in}_3\upsilon_2$ with vortex 2 placed closer to the bottom of the PST. The change in flow patterns shows that the recirculation in the region close to the inlet and its interaction with vortex 2 can be used to set the overall flow patterns for this condition.

The flow features are further analysed from velocity and turbulence profiles. This will enable more detail into the impact of geometry on the flow. The velocity and turbulent kinetic profiles profiles at lines 1, 2 and surface are analysed to compare the performance of the different inlet designs and velocities $\mathrm{in}_j\upsilon_c$.

Figure 18 shows the influence of the inlet design on the velocity at line 1. The velocity profile was normalized by the influent velocity. It is possible to observe that the centre of the vortex present in line 1 corresponds to a dead zone, where the velocities approximating $0\ \mathrm{m\ s^{-1}}$. The same is observed for both influent velocities υ_1 and υ_2 and all inlet design variations in_j. In a general visualization of the velocity profiles, it is also possible to conclude that, besides slight differences in magnitude, all simulations have a similar velocity profile at line 1.

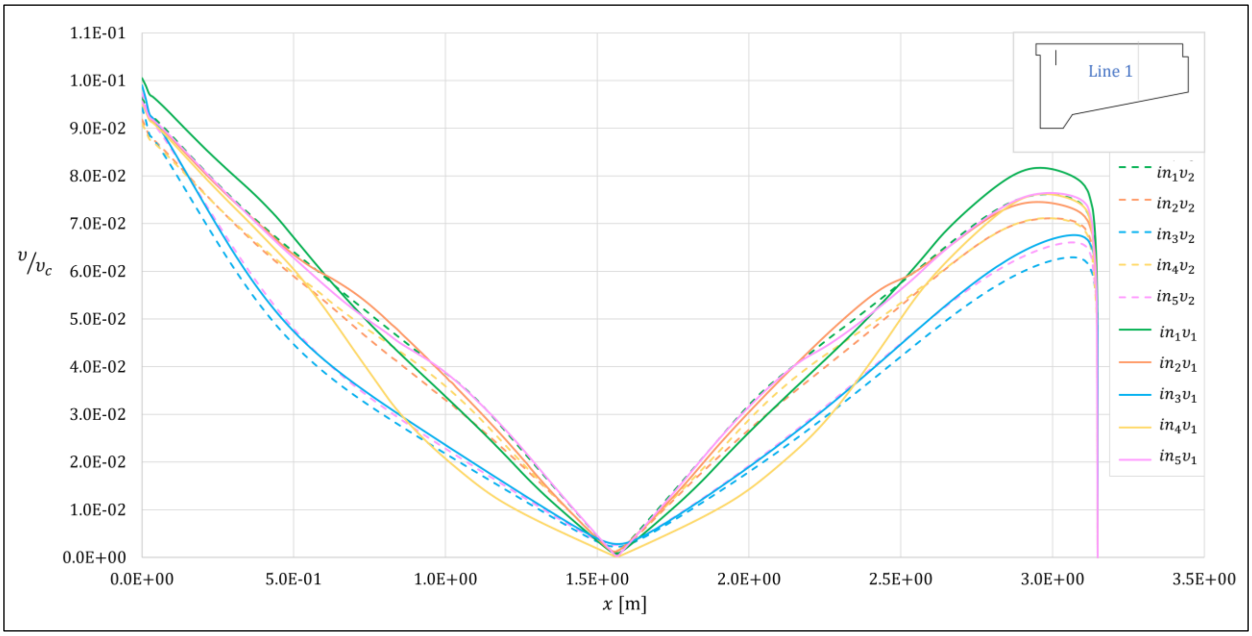

Figure 18 - Normalized velocity magnitude profile at line 1 for simulations $in_j v_c$.

To better evaluate the performance of the inlet designs and the characteristics influenced by the inlet design, the turbulent kinetic energy, k, at line 1, for each simulation $\mathrm{in_j \upsilon_c}$ is shown in Figure 19 and all the profiles were normalized by the influent velocity.

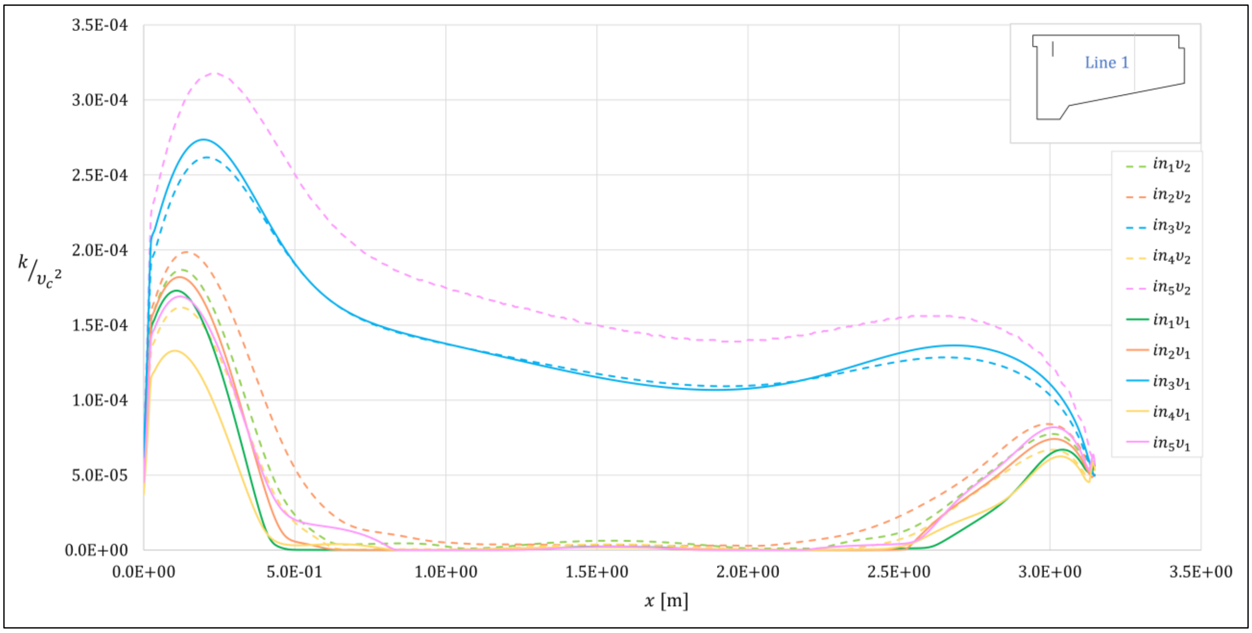

Figure 19 - Normalized turbulent kinetic energy at line 1 for simulations $in_j v_c$.

Figure 19 shows that for the highest velocity and simulations $\mathrm{in_1\upsilon_1}$, $\mathrm{in_1\upsilon_2}$, $\mathrm{in_2\upsilon_1}$, $\mathrm{in_2\upsilon_2}$, $\mathrm{in_4\upsilon_1}$, $\mathrm{in_4\upsilon_2}$ and $\mathrm{in_5\upsilon_1}$, turbulent energy is accumulated near the surface and the lower wall, with a region of relative low turbulence in the core of the large vortex closer to the outlet, where there is stagnation of the flow. On the other hand, the $\mathrm{in}_3\upsilon_1$, $\mathrm{in}_3\upsilon_2$ and $\mathrm{in}_5\upsilon_2$ conditions show a higher turbulent energy along the entire crossline 1. This is associated to the smaller gap for fluid flow over the PST that promotes a faster and more turbulent jet flowing on the surface but representing less fraction of the overall flow rate. Considering that it is desirable less turbulent energy near the bottom wall, for an efficient operation of a PST, to minimize resuspension of settled matter, the inlet designs that present better results in what concerns the k parameter are $\mathrm{in}_1\upsilon_1$, $\mathrm{in}_1\upsilon_2$, $\mathrm{in}_4\upsilon_1$ and $\mathrm{in}_4\upsilon_2$.

For the second location, line 2, the normalized velocity for each $\mathrm{in}_j\upsilon_c$ is shown in Figure 20.

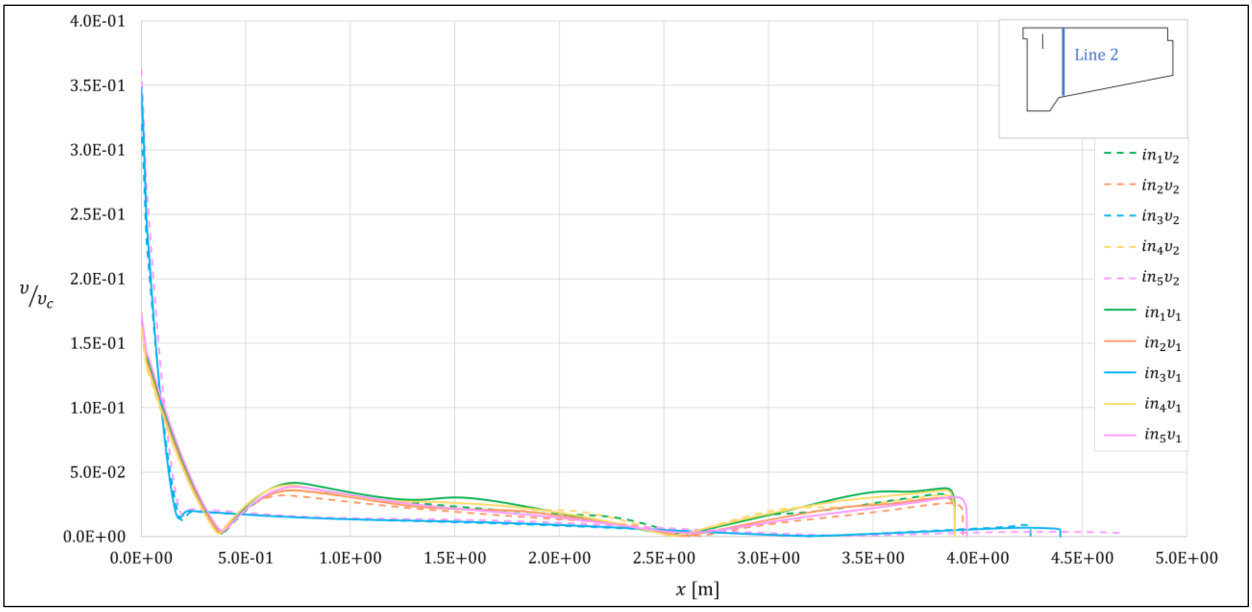

Figure 20 - Normalized velocity magnitude at line 2 for simulations $in_j\upsilon_c$.

In Figure 20, the simulations that correspond to the higher velocity gradient in line 2 are $\mathrm{in}_3\upsilon_1$, $\mathrm{in}_3\upsilon_2$ and $\mathrm{in}_5\upsilon_2$. The last condition has larger velocities near tank's surface and decrease substantially in the first 20 centimeters of the tank until an almost constant velocity throughout the rest of the tank height. These are the cases where vortex 1 is pushed to the bottom of the tank, and so the inlet jet gets dominant while the flow bellow the baffle loses dynamics.

The other simulations $\mathrm{in}_1\upsilon_1$, $\mathrm{in}_1\upsilon_2$, $\mathrm{in}_2\upsilon_1$, $\mathrm{in}_2\upsilon_2$, $\mathrm{in}_4\upsilon_1$, $\mathrm{in}_4\upsilon_2$ and $\mathrm{in}_5\upsilon_1$, show a lower velocity near the tank's surface and show a decrease of velocity in the first 50 centimeters of the tank. Comparing the inlet designs for both velocities the one that presents the best results were the ones from conditions $\mathrm{in}_3\upsilon_1$ and $\mathrm{in}_3\upsilon_2$, due to the consistency in the decrease of velocity and turbulent kinetic energy, evaluated posteriorly. For a more efficient sedimentation process, the design of the inlet and baffle play an important role in the energy dissipation, and the decrease of velocity in the settling tank. The same can be corroborated through the analysis of Figure 21 that shows the Turbulent Kinetic Energy, at line 2, for each simulation $\mathrm{in}_j\upsilon_c$.

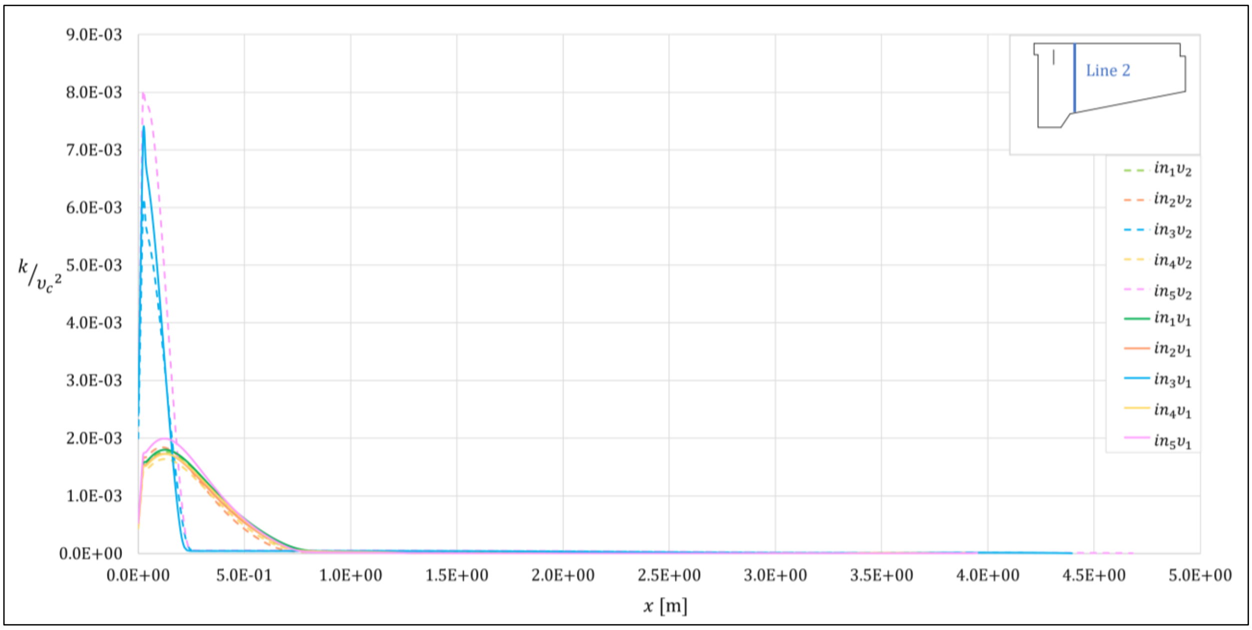

Figure 21 - Normalized turbulent kinetic energy at line 2 for simulations $in_j\upsilon_c$.

The turbulent kinetic energy is directly related to the flow dynamics, and so, the cases with faster jets are the ones with larger turbulence. This is clear in Figure 21, which closely follows the trend of the velocity profile in Figure 20.

Analysing the results at the surface, for simulations $\mathrm{in_j}\upsilon_c$, the normalized velocity and normalize turbulent kinetic energy profiles were plotted in Figure 22 and Figure 23 respectively. Comparing the normalized velocity profiles, in Figure 22, it is possible to conclude that the velocity profiles are similar for all inlet designs, except to inlet design $\mathrm{in_5}$ (simulations $\mathrm{in_5}\upsilon_1$ and $\mathrm{in_5}\upsilon_2$). The turbulent kinetic energy plot at the surface presents is similar to the velocity profiles. Simulation $\mathrm{in_3}\upsilon_2$ shows a larger value of k for the first 50 centimeters of the tank, due to smaller gap between the baffle and the surface that promotes a faster and more turbulent jet at the surface. At the same time, $\mathrm{in_3}\upsilon_1$ and $\mathrm{in_3}\upsilon_2$ simulations present lower velocities closer to the inlet, which correspond to a larger energy dissipation, required for a better operation of a PST.

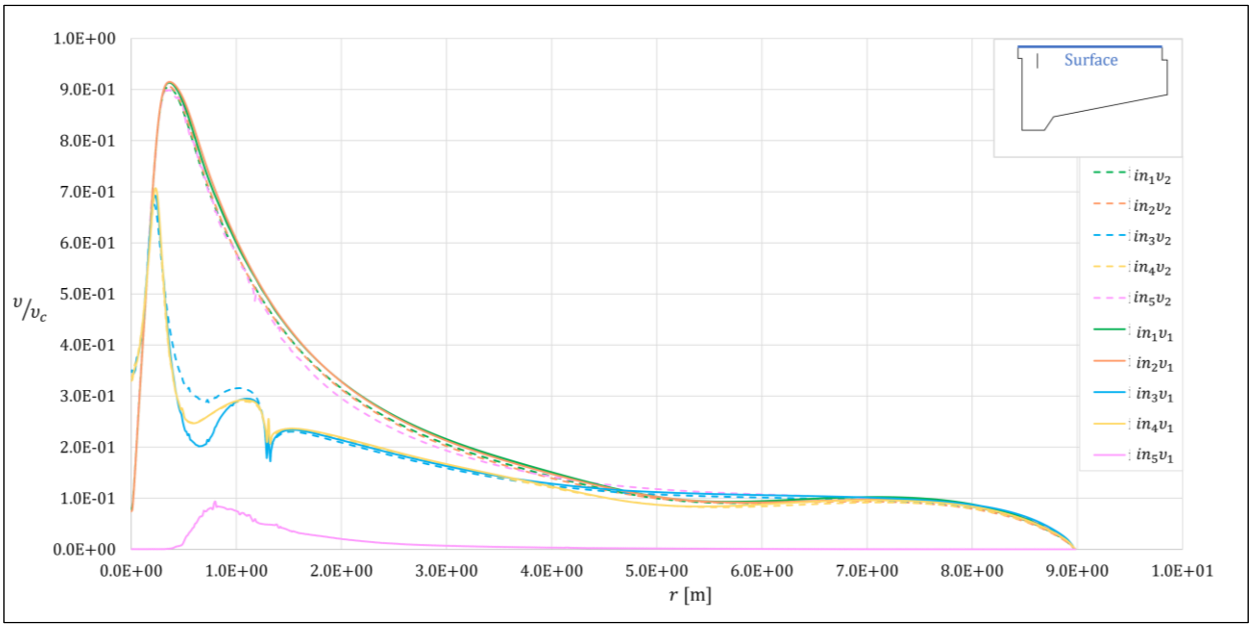

Figure 22 - Normalized surface velocity for simulations in_jv_c.

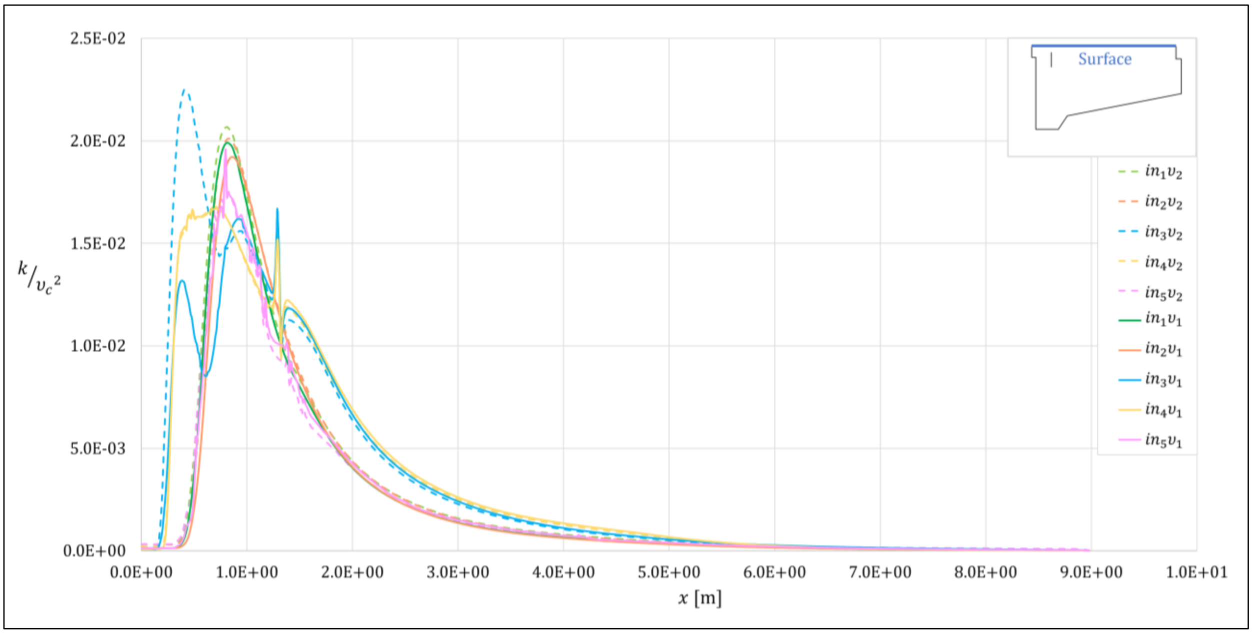

Figure 23 - Normalized surface turbulent kinetic energy for simulations in_jv_c.

4.2 CFD Results of DPM simulations

Results of DPM simulations, ϕ_i, were analyzed from the percentage of particles that remained in the PST. 1000 particles were injected ate the inlet and the conditions simulated were in_1v_1. The computational times for these simulations were approximately 36 hours.

Table 7 shows the removal's percentage [%] for the six different sized discrete particles, for the simulated flow in in_1v_1.

Table 7 - Removal percentage, for DPM simulations ϕ_i.

ϕ_i	Particle diameter $[\mathrm{m}]$	Removal $[\%]$
ϕ_1	1.0×10^{-5}	6.2
ϕ_2	2.0×10^{-5}	10.0
ϕ_3	4.0×10^{-5}	87.0
ϕ_4	1.0×10^{-4}	100.0
ϕ_5	2.0×10^{-4}	100.0
ϕ_6	1.0×10^{-3}	100.0

As shown in Table 7 the removal's percentage increases with the increase of the particle size. It reaches the value 100 % for particle's diameter of $\geq 1.0 \cdot 10^{-4}\ \mathrm{m\ s^{-1}}$. For larger sediments, the settling is faster, and the removal's percentage is higher.

4.3 Settling Expedite Assessment Method

DPM in Ansys FLUENT 2022 R1 has limitations due to the long computational time for each simulation. Therefore, a method for the prediction of the settling behaviour of particles was developed in this work. The Settling Expedite Assessment Method, SEAM, is based on the time it takes for a flow path line, δ, to go from the inlet to the outlet. Path lines were drawn, from inlet, and it was possible to understand which path lines were directly exiting through outlet 1(out_1 in Figure 8) and which ones got trapped in the two large vortices. SEAM defines that, if the terminal velocity of a particle, v_{s_i}, is higher than,

$$\boldsymbol{v}_{\delta_{n-1}\ to\ \delta_n} = \frac{\Delta \boldsymbol{h}}{\boldsymbol{\Delta t}_{\delta_n}} \tag{19}$$

the particle moves to the next path line. In Equation 19, $\Delta h = h_{\delta_n} - h_{\delta_{n-1}}$ is the distance between two path lines, and Δt_{δ_n} is the time that a path line takes to achieve the radial coordinate at the end of the free surface ($r = 9\ \mathrm{m}$). The particles that fall below the last path line that reaches the outlet get trapped in the two larger vortices, where they eventually settle to the PST's bottom. So, it is considered that the particles will settle and will not exit outlet 1 (out_1 in Figure 8). Figure 24 shows a schematic of SEAM. The terminal velocity of a particle is calculated through the Stoke's equation, described in Appendix A.

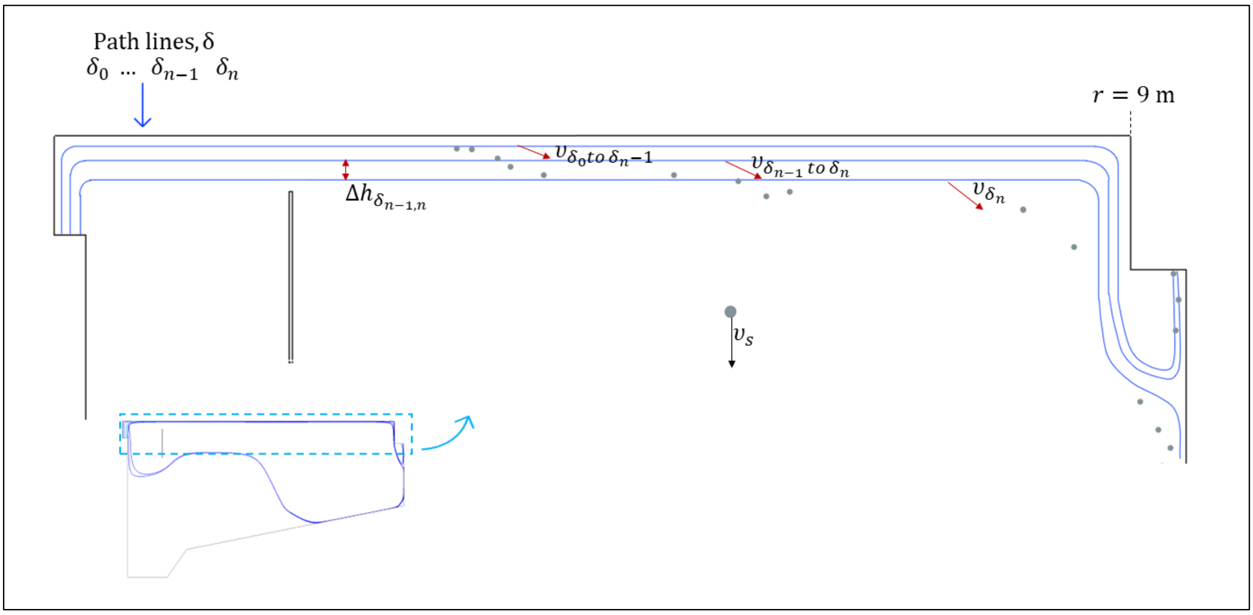

Figure 24 - Schematic of the Settling Expedite Assessment Method developed in this work.

SEAM was applied to the simulation $in_1\upsilon_1$, where 11 path lines from the inlet were created, with a spacing of 0.0175 m between them. The last path line, δ_{10}, is the path line from which all discrete particles settle. Afterwards, all the Δt_{δ_n} and $\Delta h_{\delta_n\ to\ \delta_n}$ were extracted for every path line, and every $\upsilon_{\delta_{n-1}\ to\ \delta_n}$ was calculated. These values are shown in Table 8, which also presents the flow percentage between path lines.

Table 8 - SEAM parameters obtained for simulation $in_1\upsilon_1$.

δ_n	Initial inlet point r [m]	Δt_{δ_n} [s]	$\Delta h_{\delta_n\ to\ \delta_n}$		$\upsilon_{\delta_{n-1}\ to\ \delta_n}$ [m s^{-1}]	Flow $\delta_{n-1}\ to\ \delta_n$ %
			Interval	[m]		
δ_0	0.0000	42.2	δ_0 to δ_1	1.14×10^{-4}	2.70×10^{-6}	1
δ_1	0.0175	42.3	δ_1 to δ_2	1.37×10^{-4}	3.24×10^{-6}	3
δ_2	0.0350	47.0	δ_2 to δ_3	3.44×10^{-3}	7.32×10^{-5}	6
δ_3	0.0525	44.0	δ_3 to δ_4	1.97×10^{-3}	4.48×10^{-5}	8
δ_4	0.0700	45.2	δ_4 to δ_5	4.44×10^{-3}	9.82×10^{-5}	10
δ_5	0.0875	43.5	δ_5 to δ_6	3.01×10^{-3}	2.70×10^{-6}	13
δ_6	0.1050	43.0	δ_6 to δ_7	3.80×10^{-3}	8.84×10^{-5}	15
δ_7	0.1225	43.0	δ_7 to δ_8	4.05×10^{-3}	9.42×10^{-5}	17
δ_8	0.1400	42.6	δ_8 to δ_9	4.31×10^{-3}	1.10×10^{-4}	19
δ_9	0.1575	42.9	δ_9 to δ_{10}	3.82×10^{-3}	8.90×10^{-5}	22
δ_{10}	0.1750					

Then, to evaluate the settling of different discrete particle's sizes, the terminal velocities for 6 different particle diameters were calculated, through the Stoke's equation (Equation A.3 from Appendix A) and considering the particle material is Anthracite ($\rho_A = 1200 \text{ kg m}^{-3}$). The terminal velocities, υ_{s_i}, are shown in Table 9.

Table 9 - Discrete particles diameter and terminal velocities.

ϕ_i	Diameter [m]	υ_{s_i} [m s^{-1}]
ϕ_1	1.0×10^{-5}	1.10×10^{-5}
ϕ_2	2.0×10^{-5}	4.40×10^{-5}
ϕ_3	4.0×10^{-5}	1.85×10^{-4}
ϕ_4	1.0×10^{-4}	1.10×10^{-3}
ϕ_5	2.0×10^{-4}	4.40×10^{-3}
ϕ_6	1.0×10^{-3}	1.10×10^{-1}

With the terminal velocities for each different particle size, υ_{s_i} and $\upsilon_{\delta_{n-1}\ to\ \delta_n}$, it is possible to calculate the percentage of particles that stays in the tank and how many particles go from one path line to another i.e. if $\upsilon_{s_i} > \upsilon_{\delta_{n-1}\ to\ \delta_n}$, then the particles i in the flow that is in between path lines δ_{n-1} to δ_n settle. For example, from Tables 8 and 9 it is possible to perceive that particles ϕ_1 and ϕ_2, do not settle for this particular flow; 22 % of the particles ϕ_3 would settle, because $\upsilon_{s_3} > \upsilon_{\delta_9\ to\ \delta_{10}}$, and 100 % of particles ϕ_4, ϕ_5 and ϕ_6 would settle for this flow, since their terminal velocities are larger than all velocities $\upsilon_{\delta_{n-1}\ to\ \delta_n}$. In Appendix B, can be found a more extensive explanation of SEAM for this flow and discrete particle diameters.

In sum, SEAM describes a simpler method of predicting the sedimentation for discrete particles, than DPM in Ansys Fluent. In SEAM some considerations must be taken into account: a homogeneous distribution of particles throughout the flow; each path line will vary in accordance with the influent velocity, as such, for each different influent velocity, new path lines must be created. The turbulence is considered homogeneous, i.e. the turbulence fluctuations net effect is annulled and there is no lift or falling of the particle due to small eddies. Close to the surface, this is an assumption that has some limitations, but it was kept for the sake of the simplicity of the method.

4.3.1 DPM simulation versus SEAM

For a further study of DPM simulations and SEAM method it is relevant to compare both the results for the removal's percentage of the DPM simulation (Table 7) and the results of SEAM for the particle's size present in Table 9. For particles with a diameter larger than 1.0×10^{-4} m both methods predict a removal of 100 % of particles, considering the flow simulated in $\mathrm{in}_1\upsilon_1$. For particles with the diameter 4.0×10^{-5} m SEAM predicts a removal of 22 % of the particles, while DPM simulation presented a value of 87 % for this diameter. For the two smaller particle diameters, 1.0×10^{-5} and 2.0×10^{-5} m, SEAM predicts that all particles exit through outlet 1, while the removal's percentage determined from DPM simulations are of 6.2 and 10.0 %, respectively for each diameter. These differences can be a result of simplifications considered in the development of SEAM. Even though both methods generally predict the full retention of particles with a diameter larger than 4.0×10^{-5} m.

4.3.2 Application of SEAM to a PST case study

SEAM can be applied to a PST cases study for wastewater treatment. The settling behaviour of a Particle Size Distribution (PSD) of MLSS of a wastewater was studied using SEAM. A typical PSD from a sludge in a bioreactor was obtained at middle position by Pang et al., 2020. This PSD is used to investigate the to investigate the fouling mechanism of membrane in an anaerobic membrane bioreactor, installed at different heights in reactors (Chao Pang 2020). The settled particle's percentages as well as the final effluent concentration are calculated. For the purpose of this study, it was used the middle position PSD and the data from simulation $\mathrm{in}_1\upsilon_1$, detailed in the previous section (Section 4.3,Table 8).

The terminal velocities of the different particle sizes, υ_s, were calculated and compared with the SEAM parameters for simulation $\mathrm{in}_1\upsilon_1$. Figure 25 shows the percentage of particles that settle for the PSD case study.

The concentration of suspended solids, SS, in the influent at the PST inlet is $500\ \mathrm{mg\,L^{-1}}$. The particle size distribution and settling percentages are in Figure 25. The effluent that exists outlet 1 has a SS concentration of $413\ \mathrm{mg\,L^{-1}}$, which represents a removal of 17 %. This low percentage removal can be justified from the high inlet velocity ($2.2\ \mathrm{m\,s^{-1}}$) and the simplification of using a discrete settling behaviour instead of a flocculent settling behaviour.

Then, to analyse the influence of the influent velocity on the settling behaviour of the PSD, the SEAM parameters for simulation $\mathrm{in}_1\upsilon_2$ were obtained, shown in Appendix C, and the settling percentages accordingly to this flow were determined. Figure 26 shows the percentage of particles that settle for the PSD studied and the influent velocity υ_2. Considering the concentration of suspended solids, SS, in the influent is $500\ \mathrm{mg\,L^{-1}}$, the PSD and settling percentages in Figure 26, the effluent that exists outlet 1 has a SS concentration of $402\ \mathrm{mg\,L^{-1}}$, which corresponds to a removal's percentage of 20 % of the influent mass. These results show that the influent velocity translates directly into the removal percentage of the SS concentration on the PST. For the larger sediments and the smaller the velocity, the removal's percentage is higher.

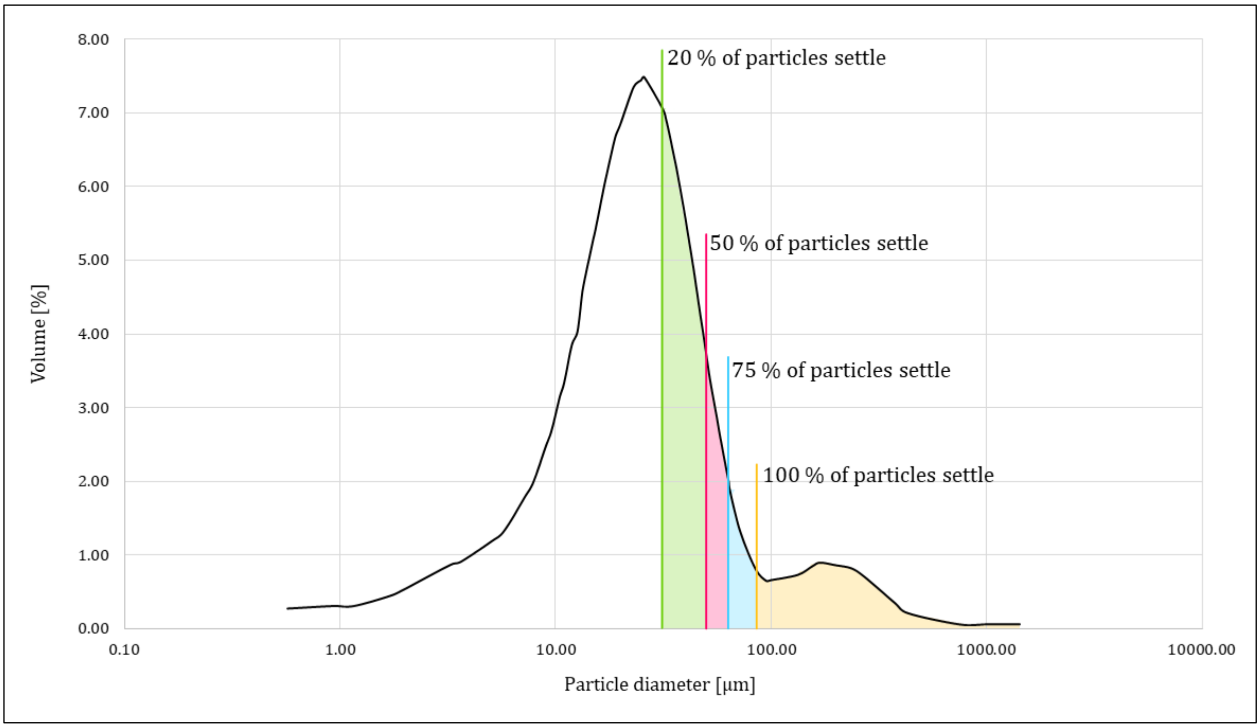

Figure 25 - Typical PSD of a bioreactor sludge and settling percentages according to SEAM for in_1v_1.

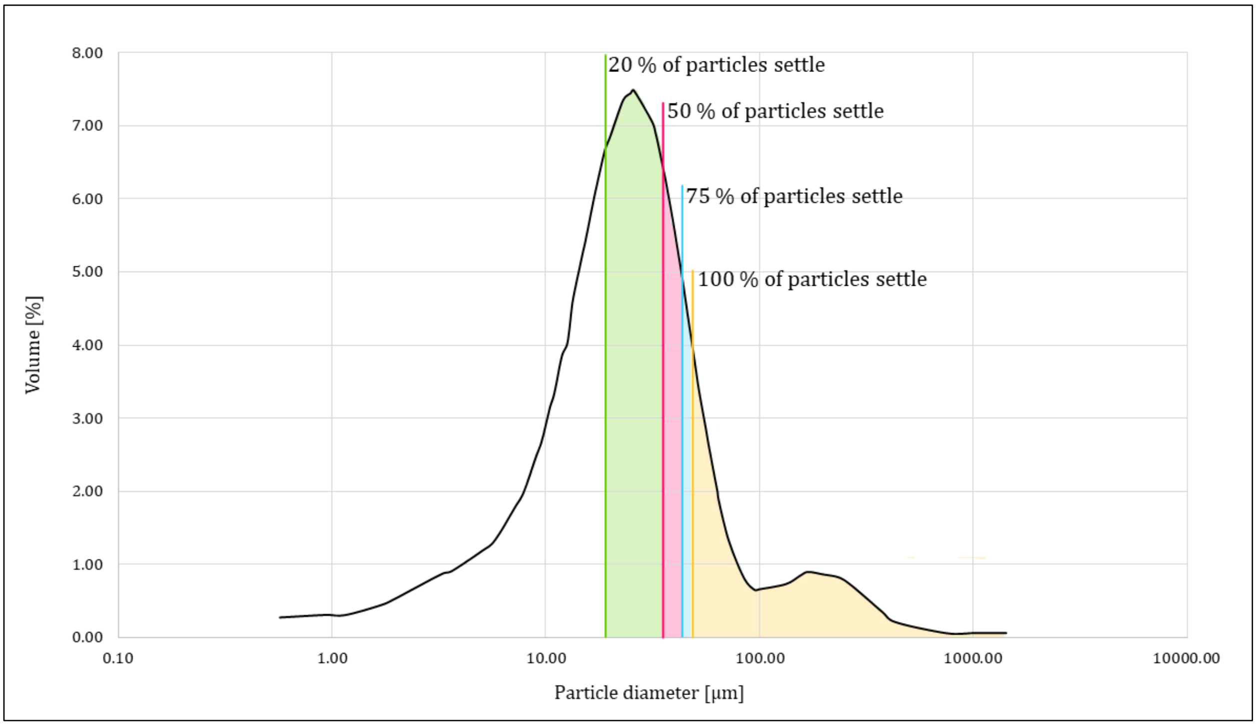

Figure 26 - Typical PSD of a bioreactor sludge and settling percentages according to SEAM for in_1v_2.

5 Conclusion

The efficiency of a primary settling tank has a fundamental role in what concerns the goal of energetic sustainability of a wastewater treatment plant. The development of flexible methods for the conception of more efficient and better adapted PSTs becomes a pressing matter to fulfil mitigating actions in the wastewater sector, aiming toward Net-Zero Energy and Net-Zero Carbon targets.

CFD fills a void in the development of PSTs, enabling a holistic study of the various components of the settling unit and, at the same time, the integration of models for the study of both hydrodynamics and settling behaviours. CFD models can contribute to further design optimization in downstream unit processes at WWTPs. This thesis fits in the studies developed for a WWTP in the South Coast of England.

Different inlet and baffle designs were studied using steady state CFD simulations. The defined parameters for efficiency analysis were the Turbulent Kinetic Energy and the inlet velocity. Results show that PST with the baffle's position closer to the free surface for both inlet velocities, $2.2 \text{ m } s^{-1}$ and $1.0 \text{ m } s^{-1}$ (conditions $\text{in}_3\upsilon_1$ and $\text{in}_3\upsilon_2$) is the one that presents the best efficiency according to the hydrodynamics.

For one of the simulated hydrodynamic conditions, named in this work as $\text{in}_1\upsilon_1$, DPM simulations were performed using ANSYS Fluent. Six different particle sizes were injected in the inlet and their trajectory inside the PST was tracked. These simulations results were analysed through the removal's percentage of particles, which is the percentage of particles that stays in the tank. It was possible to conclude that for diameters $\geq 1.0 \times 10^{-4}$ m, 100 % of particles settle.

A method called SEAM was developed to study the settling behaviour of particles using Stoke's law. This method was applied to the steady-state simulation for the condition $\text{in}_1\upsilon_1$. The same behaviour observed through the DPM simulations was obtained from SEAM, i.e., all particles with diameters $\geq 1.0 \times 10^{-4}$ m, all settle. SEAM also shows that the initial particle position, their size and the flow's hydrodynamics are the parameters responsible by the settling behaviour of the particles.

SEAM was also applied to case study using a particle size distribution reported in the literature (Chao Pang 2020). The removal's percentage determined from SEAM and using the literature's data was lower than the percentages reported in wastewater treatment plants.

CFD models developed in this work enable a better understanding of the influence of velocity and geometric variations in the hydrodynamics of a circular primary settling. This thesis will contribute to further know-how of the design concept and optimization of PSTs in WWTPs, guaranteeing the achievement of higher sedimentation efficiencies.

5.1 Limitations and Future Work

During this thesis' work, the main limitation was the required simulation time. The validation of the mesh didn't allow much time for the improvement of the final results as well as the exploration of different approaches and models for the simulation of the sedimentation processes within PST case study.

On the other hand, the learning of the software, Ansys Fluent, was also a time consuming process, since this software and the theory behind it were not subjects of study prior to this work, increasing the difficulty of the fulfilment of the objectives of this work.

In the future, there are a few different views that could be interesting to explore: study of more advanced turbulence model, namely Large Eddy Simulation for the numerical validation of RANS; cover a wider range of designs at the inlet to dissipate the short-circuit flow from inlet to outlet; the adaptation of SEAM for a flocculent type settling behaviour and the simulation of the suspended solids using an Euller-Euller approach, granular flow, that enables more advanced modelling of the sedimentation.

6 References

Abdel-Gawad, Sameh M, and John A McCorquodale. 1984. 'Strip integral method applied to settling tanks', *Journal of Hydraulic Engineering*, 110: 1-17.

Ansys, Inc. 2022. *Ansys Fluent Theory Guide*.

Camp, T. R. 1953. 'Studies of Sedimentation Basin Design'.

Chao Pang, Xuesong Ren, Xuedong Zhang, Zhenhu Hu, Wei Wang. 2020. 'Influence of immersion depth of membrane on filtration

performance of anaerobic membrane bioreactor', *Environmental Science and Pollution Research*.

Cheng Sun, Liang Guo, Yongkang Zheng, Dan Yu, Chunji Jin, Yangguo Zhao, Zhiwen Yao, Mengchun Gao, Zonglian She,. 2022. 'Effect of mixed primary and secondary sludge for two-stage anaerobic digestion (AD)', *Bioresource Technology*, 343.

Griborio, Alonso, J Alex McCorquodale, and Jenny A Rodriguez. 2014. 'CFD modeling of primary clarifiers: the state-of-the-art', *Proceedings of the Water Environment Federation*, 2014: 1926-49.

Hendricks, David. 2016. *Fundamentals of water treatment unit processes: physical, chemical, and biological* (Crc Press).

Hreiz, Rainier, M. A. Latifi, and Nicolas Roche. 2015. 'Optimal design and operation of activated sludge processes: State-of-the-art', *Chemical Engineering Journal*, 281: 900-20.

Imam, E., McCorquodale, J. A. & Bewtra, J. K. 1983. 'Numerical modelling of sedimentation tanks', *Journal of Hydraulic*

Engineering, 109.

International Energy Agency, INE. 2021. "Net Zero by 2050 - A Roadmap for the Global energy sector." In.

Larsen, P. 1977. *On the Hydraulics of Rectangular Settling Basins: Experimental and Theoretical Studies* (Department of Water Resources Engineering, Lund Institute of Technology, University of Lund).

Laurent, J., R. W. Samstag, J. M. Ducoste, A. Griborio, I. Nopens, D. J. Batstone, J. D. Wicks, S. Saunders, and O. Potier. 2014. 'A protocol for the use of computational fluid dynamics as a supportive tool for wastewater treatment plant modelling', *Water Science and Technology*, 70: 1575-84.

Margarit Bel, Nuria, Cesar Retana Pastor, and Jorge J Malfeito Sanchez. 2017. 'Reducing both CAPEX and OPEX thanks to CFD at Gabal-el-Asfar WWTP: hydraulic optimization of flow distribution to clarifiers and sedimentation tanks', *Desalination and Water Treatment*, 68: 310-18.

Mazzolani, G., F. Pirozzi, and G. d'Antonoi. 1998. 'A generalized settling approach in the numerical modeling of sedimentation tanks', *Water Science and Technology*, 38: 95-102.

Metcalf, and Eddy. 2014. *WASTEWATER ENGINEERING: TREATMENT AND RESOURCE RECOVERY*.

Patziger, Miklos, Frank Wolfgang Günthert, Norbert Jardin, Harald Kainz, and Jörg Londong. 2016. 'On the design and operation of primary settling tanks in state of the art wastewater treatment and water resources recovery', *Water Science and Technology*, 74: 2060-67.

Patziger, Miklós, and Katalin Kiss. 2015. 'Analysis of suspended solids transport processes in primary settling tanks', *Water Science and Technology*, 72: 1-9.

Samstag , R W, J J Ducoste , A Griborio , and Ingmar Batstone Nopens , DJ Wicks, JD Saunders , S Wicklein , EA Kenny , G Laurent , J. 2016. 'CFD for wastewater treatment: an overview', *Water Science and Technology*, 74: 549-63.

Sonune, Amit, and Rupali Ghate. 2004. 'Developments in wastewater treatment methods', *Desalination*, 167: 55-63.

Takamatsu, Takeichiro, Masaaki Naito, Sadataka Shiba, and Yasuyo Ueda. 1974. 'Effects of Deposit Resuspension on Settling Basin', *Journal of the Environmental Engineering Division*, 100: 883-903.

Wang , Lian-Ping, and Martin R. Maxey 1993. 'Settling velocity and concentration distribution of heavy particles in homogeneous isotropic turbulence', *Journal of Fluid Mechanics*, 256: 27-68.

Wicklein, Edward, Damien J. Batstone, Joel Ducoste, Julien Laurent, Alonso Griborio, Jim Wicks, Stephen Saunders, Randal Samstag, Olivier Potier, and Ingmar Nopens. 2015. 'Good modelling practice in applying computational fluid dynamics for WWTP modelling', *Water Science and Technology*, 73: 969-82.

Xanthos, Savvas, Minwei Gong, Krish Ramalingam, John Fillos, Alan Deur, Keith Beckmann, and John Alexander McCorquodale. 2011. 'Performance Assessment of Secondary Settling Tanks Using CFD Modeling', *Water Resources Management*, 25: 1169-82.

Zhang, Duo. 2014. 'Optimize sedimentation tank and lab flocculation unit by CFD', Norwegian University of Life Sciences.

Appendix A – Stoke's Law

Particle settling is based on the principle represented by the Stokes law.

In Figure 27 is represented a free body diagram for a falling particle in dynamic equilibrium, which means the drag force, F_D, is equal to the propulsion force, or buoyant weight W_B.

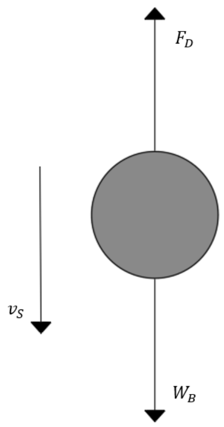

Figure 27 - Free body diagram of a particle and its acting forces.

The buoyant weight is given by the expression,

$$F_D = W_B = V(\rho_p - \rho_f)g \tag{A.1}$$

Where V is the water displaced by particle ($\mathrm{m^3}$), ρ_p is the specific mass of particle ($\mathrm{kg\,m^{-3}}$), ρ_f is the specific mass of fluid medium ($\mathrm{kg\,m^{-3}}$), and g is the acceleration of gravity ($9{,}8\ \mathrm{m\,s^{-2}}$).

The drag force, F_D represented by Equation 2, is caused, in a turbulent flow, by boundary shear and unequal pressure distribution around the object. In a laminar flow, it's due to the viscous shear forces that are distributed through the fluid.

$$F_D = C_D \rho A \frac{v_s^2}{2} \tag{A.2}$$

Where, C_D is the drag coefficient, A is the projected area of the particle ($\mathrm{m^2}$), ρ is the fluid's density ($\mathrm{kg\,m^{-3}}$) and v_s is the particle's terminal velocity ($\mathrm{m\,s^{-1}}$).

The drag coefficient is obtained through the Reynolds number ($C_D = \frac{24}{\mathrm{Re}}$) and considering that, in a dynamic equilibrium, the drag forces equals the propulsion forces and that the particles structure is similar to a sphere, Equation 3 expresses Stokes Law.

$$v_s = \frac{1}{18}\frac{g}{v}(\rho_p - \rho_f)D^2 \tag{A.3}$$

Where, v is the kinematic viscosity of the fluid ($\mathrm{m^2\,s^{-1}}$).

Appendix B – Settling Expedite Assessment Method

In this appendix, it was intended to provide a detailed explanation of the Settling Expedite Assessment Method, SEAM, for the case exposed in chapter 4, section 4.3. To demonstrate this method, the time taken by each different particle to go from a path line to the next was calculated. Posteriorly, it was summed the total time it would take a particle from each path line to the last path line δ_n, where it is considerer that all particles that arrive to δ_n settle. Finally, if the total time for each particle was smaller than $\Delta t_{\delta_{n-1}\,to\,\delta_n}$, it was considered that the particle passed to the next path line.

The value of all $\Delta t_{\delta_{n-1}\,to\,\delta_n}$ for each particle size, was obtain through the following expression,

$$\Delta t_{\delta_{n-1}\,to\,\delta_n} = \frac{\Delta h_{\delta_n\,to\,\delta_n}}{v_{s_i}} \quad \text{(B.1)}$$

Table B 1 presents the results $\Delta t_{\delta_{n-1}\,to\,\delta_n}$ and all calculations were performed based in the values presented in Tables 9 and 10.

Table B 1 – Time it takes for a discrete particle to go from path line δ_{n-1} to δ_n.

ϕ_i	$\Delta t_{\delta_0\,to\,\delta_1}$	$\Delta t_{\delta_1\,to\,\delta_2}$	$\Delta t_{\delta_2\,to\,\delta_3}$	$\Delta t_{\delta_3\,to\,\delta_4}$	$\Delta t_{\delta_4\,to\,\delta_5}$	$\Delta t_{\delta_5 to\,\delta_6}$	$\Delta t_{\delta_6\,to\,\delta_7}$	$\Delta t_{\delta_7\,to\,\delta_8}$	$\Delta t_{\delta_8\,to\,\delta_9}$	$\Delta t_{\delta_9\,to\,\delta_{10}}$
ϕ_1	1.04×10^1	1.25×10^1	3.13×10^2	1.79×10^2	4.04×10^2	2.74×10^2	3.46×10^2	3.68×10^2	3.92×10^2	3.47×10^2
ϕ_2	2.59×10^0	3.11×10^0	7.82×10^1	4.48×10^1	1.01×10^2	6.84×10^1	8.64×10^1	9.20×10^1	9.80×10^1	8.68×10^1
ϕ_3	6.16×10^{-1}	7.41×10^{-1}	1.86×10^1	1.06×10^1	2.40×10^1	1.63×10^1	2.05×10^1	2.19×10^1	2.33×10^1	2.06×10^1
ϕ_4	1.04×10^{-2}	1.25×10^{-1}	3.13×10^0	1.79×10^0	4.04×10^0	2.74×10^0	3.46×10^0	3.68×10^0	3.92×10^0	3.47×10^0
ϕ_5	2.59×10^{-2}	3.11×10^{-2}	7.82×10^{-1}	4.48×10^{-1}	1.01×10^0	6.84×10^{-1}	8.64×10^{-1}	9.21×10^{-1}	9.80×10^{-1}	8.68×10^{-1}
ϕ_6	1.04×10^{-3}	1.25×10^{-3}	3.13×10^{-2}	1.79×10^{-2}	4.04×10^{-2}	2.74×10^{-2}	3.45×10^{-2}	3.68×10^{-2}	3.92×10^{-2}	3.47×10^{-2}

The time for each different particle to go from a path line δ_n to δ_{10} was obtained through the sum of each time from path line δ_n to δ_{10}. These values are shown in *Table B 2*.

Considering the values of Δt_{δ_n} with the values obtained for each particle size's time of fall from a *path line* δ_n *to* δ_{10}, it is possible to observe, in Table B 2, that, for the particle's size 4, 5 and 6, all $\sum \Delta t_{\delta_n\,to\,\delta_{10}} > \Delta t_{\delta_n}$, which means that 100 % of these particles present in the influent flow would settle for this particular simulated flow, $in_1 v_1$. For the particles 3, only the particles present between path lines 9 and 10 would settle, so 22 % of the particles of the size 3 would settle for this particular flow. Regarding particle sizes 1 and 2, and particle sizes 3 from path lines 0 to 8, these would exist the PST through the outlet 1, not settling.

Table B 2 - Cumulative time from path line δ_n to path line 10 δ_{10}.

ϕ_i	$[s]$									
	$\sum \Delta t_{\delta_0\ to\ \delta_{10}}$	$\sum \Delta t_{\delta_1\ to\ \delta_{10}}$	$\sum \Delta t_{\delta_2\ to\ \delta_{10}}$	$\sum \Delta t_{\delta_3\ to\ \delta_{10}}$	$\sum \Delta t_{\delta_4\ to\ \delta_{10}}$	$\sum \Delta t_{\delta_5\ to\ \delta_{10}}$	$\sum \Delta t_{\delta_6\ to\ \delta_{10}}$	$\sum \Delta t_{\delta_7\ to\ \delta_{10}}$	$\sum \Delta t_{\delta_8\ to\ \delta_{10}}$	$\sum \Delta t_{\delta_9\ to\ \delta_{10}}$
ϕ_1	2.65×10^3	2.63×10^3	2.62×10^3	2.31×10^3	2.13×10^3	1.73×10^3	1.45×10^3	1.11×10^3	7.39×10^2	3.47×10^2
ϕ_2	6.61×10^2	6.59×10^2	6.55×10^2	5.77×10^2	5.33×10^2	4.32×10^2	3.63×10^2	2.77×10^2	1.85×10^2	8.68×10^1
ϕ_3	1.57×10^2	1.57×10^2	1.56×10^2	1.37×10^2	1.27×10^2	1.03×10^2	8.64×10^1	6.58×10^1	4.39×10^1	2.06×10^1
ϕ_4	2.65×10^1	2.63×10^1	2.62×10^1	2.31×10^1	2.13×10^1	1.73×10^1	1.45×10^1	1.11×10^1	7.39×10^0	3.47×10^0
ϕ_5	6.61×10^0	6.59×10^0	6.56×10^0	5.77×10^0	5.33×10^0	4.32×10^0	3.63×10^0	2.77×10^0	1.85×10^0	8.68×10^{-1}
ϕ_6	2.64×10^{-1}	2.63×10^{-1}	2.62×10^{-1}	2.31×10^{-1}	2.13×10^{-2}	1.73×10^{-1}	1.45×10^{-1}	1.11×10^{-1}	7.39×10^{-2}	3.47×10^{-2}

Appendix C – SEAM parameters for simulation in_1v_2

The SEAM parameters for simulation in_1v_2, were obtained using the same procedure described in Section 4.3. Table C 1shows these parameter's values.

Table C 1 - SEAM parameters obtained for simulation in_1v_2.

δ_n	Initial inlet point r [m]	Δt_{δ_n} [s]	$\Delta h_{\delta_n \, to \, \delta_n}$ Interval	$\Delta h_{\delta_n \, to \, \delta_n}$ [m]	$v_{\delta_{n-1} \, to \, \delta_n}$ [$\mathrm{m \cdot s^{-1}}$]	Flow δ_{n-1} *to* δ_n %
δ_0	0.0000	100.0	δ_0 to δ_1	1.30×10^{-4}	1.30×10^{-6}	1
δ_1	0.0175	98.4	δ_1 to δ_2	1.00×10^{-3}	1.02×10^{-5}	3
δ_2	0.0350	105.1	δ_2 to δ_3	1.48×10^{-3}	1.41×10^{-5}	6
δ_3	0.0525	100.8	δ_3 to δ_4	1.95×10^{-3}	1.94×10^{-5}	8
δ_4	0.0700	98.4	δ_4 to δ_5	2.45×10^{-3}	2.49×10^{-5}	10
δ_5	0.0875	97.0	δ_5 to δ_6	3.01×10^{-3}	3.10×10^{-5}	13
δ_6	0.1050	96.0	δ_6 to δ_7	3.75×10^{-3}	3.91×10^{-5}	15
δ_7	0.1225	95.2	δ_7 to δ_8	3.89×10^{-3}	4.09×10^{-5}	17
δ_8	0.1400	95.1	δ_8 to δ_9	4.23×10^{-3}	4.45×10^{-5}	19
δ_9	0.1575	96.0	δ_9 to δ_{10}	3.67×10^{-3}	3.82×10^{-5}	22
δ_{10}	0.1750					